Supporting Information for:

Bespoke Pretargeted Nano-Radioimmunotherapy for the Treatment of Non-Hodgkin Lymphoma

Kin Man Au,[1,2] Ashutosh Tripathy,[3] Carolina Pe-I Lin,[4] Kyle Wagner,[1,2] Seungpyo Hong,[5] Andrew Z. Wang,[1,2]* Steven I. Park[6,7]*

[1] Laboratory of Nano- and Translational Medicine, Carolina Center for Cancer Nanotechnology Excellence, Carolina Institute of Nanomedicine, University of North Carolina at Chapel Hill, Chapel Hill, NC 27599, USA.

[2] Department of Radiation Oncology, Lineberger Comprehensive Cancer Center, University of North Carolina at Chapel Hill, Chapel Hill, NC 27599, USA.

[3] Department of Biochemistry and Biophysics, UNC Marcomolecular Interactions Facility, 1124 Genome Science Building, 250 Bell Tower Drive, Chapel Hill, NC 27599, USA.

[4] Department of Microbiology and Immunology, University of North Carolina, Chapel Hill, North Carolina, Chapel Hill, NC 27599, USA.

[5] School of Pharmacy, University of Wisconsin, 777 Highland Ave., Madison, WI 53705, USA.

[6] Division of Hematology and Oncology, Levine Cancer Institute, Carolinas HealthCare System, 100 Medical Park Dr, Suite 110, Concord, NC 28025, USA.

[7] Lineberger Comprehensive Cancer Center, University of North Carolina at Chapel Hill, Chapel Hill, NC 27599, USA.

*Correspondence should be addressed to zawang@med.unc.edu (A.Z.W.) or steven.park@carolinashealthcare.org (S.I.P.).

SUPPORTING FIGURES

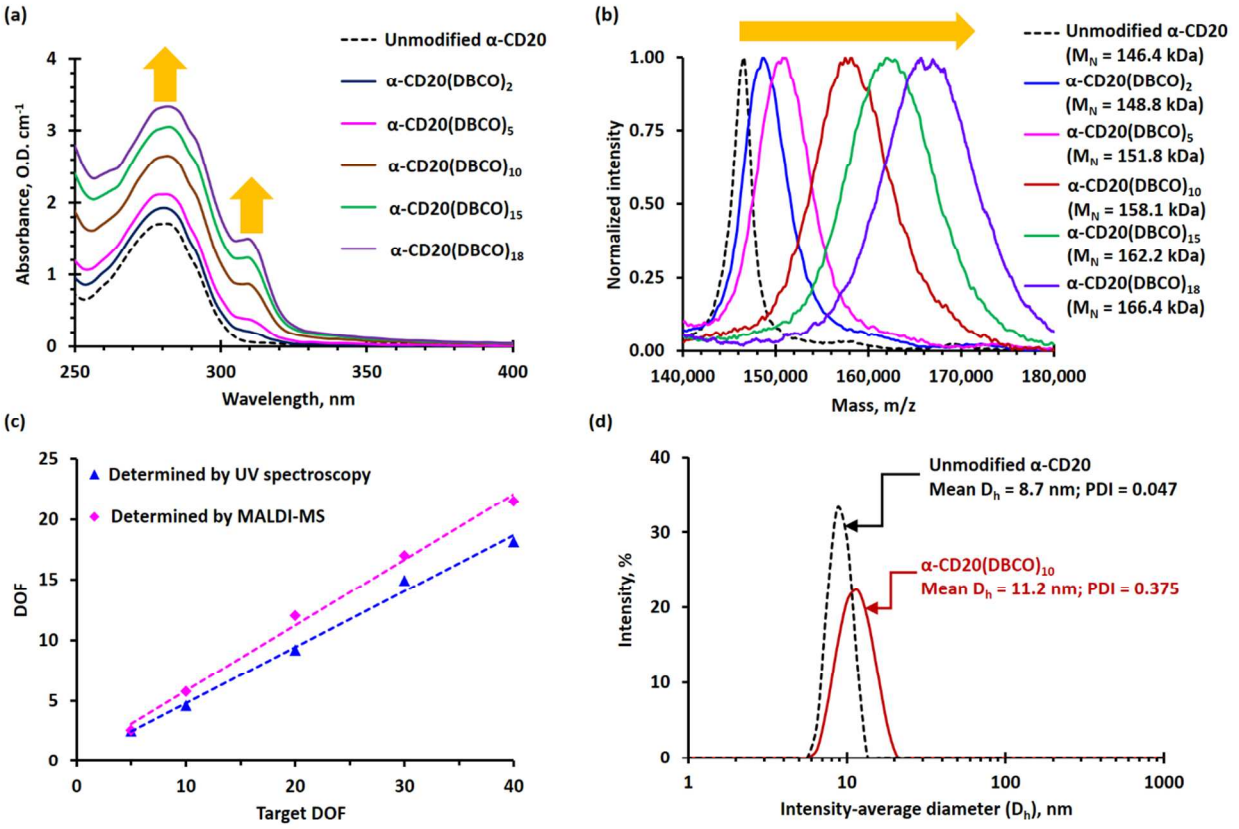

Figure S1. Characterization of DBCO-functionalized Rituximab. (a) UV spectra of 1 mg/mL (6.95 μM) of unmodified Rituximab and DBCO-functionalized α-CD20 with different degrees of functionalization (α-CD20(DBCO)$_f$, f = degree of functionalization determined by UV-visible spectroscopy). The UV absorption band at 310 nm corresponds to absorbance from the conjugated DBCO group. (b) MALDI-TOF mass spectra of unmodified α-CD20 and different samples of DBCO-functionalized α-CD20, and their number-average molecular weight (M_n) determined by MALDI-TOF mass spectroscopy. (c) The plot of DOF of different DBCO-functionalized α-CD20 determined by UV spectroscopic method and MALDI-MS versus the molar equivalent of DBCO-EG$_{13}$-NHS ligand used in the functionalization of α-CD20 (i.e., target TOF). The DOFs determined using the MALDI-TOF MS method were higher than those determined by UV spectroscopy because only 90 mol% of the DBCO-EG$_{13}$-NHS was functionalized with DBCO. (d) Intensity-average diameters (D_h) of unmodified rituximab and α-CD20(DBCO)$_{10}$, as determined by DLS method.

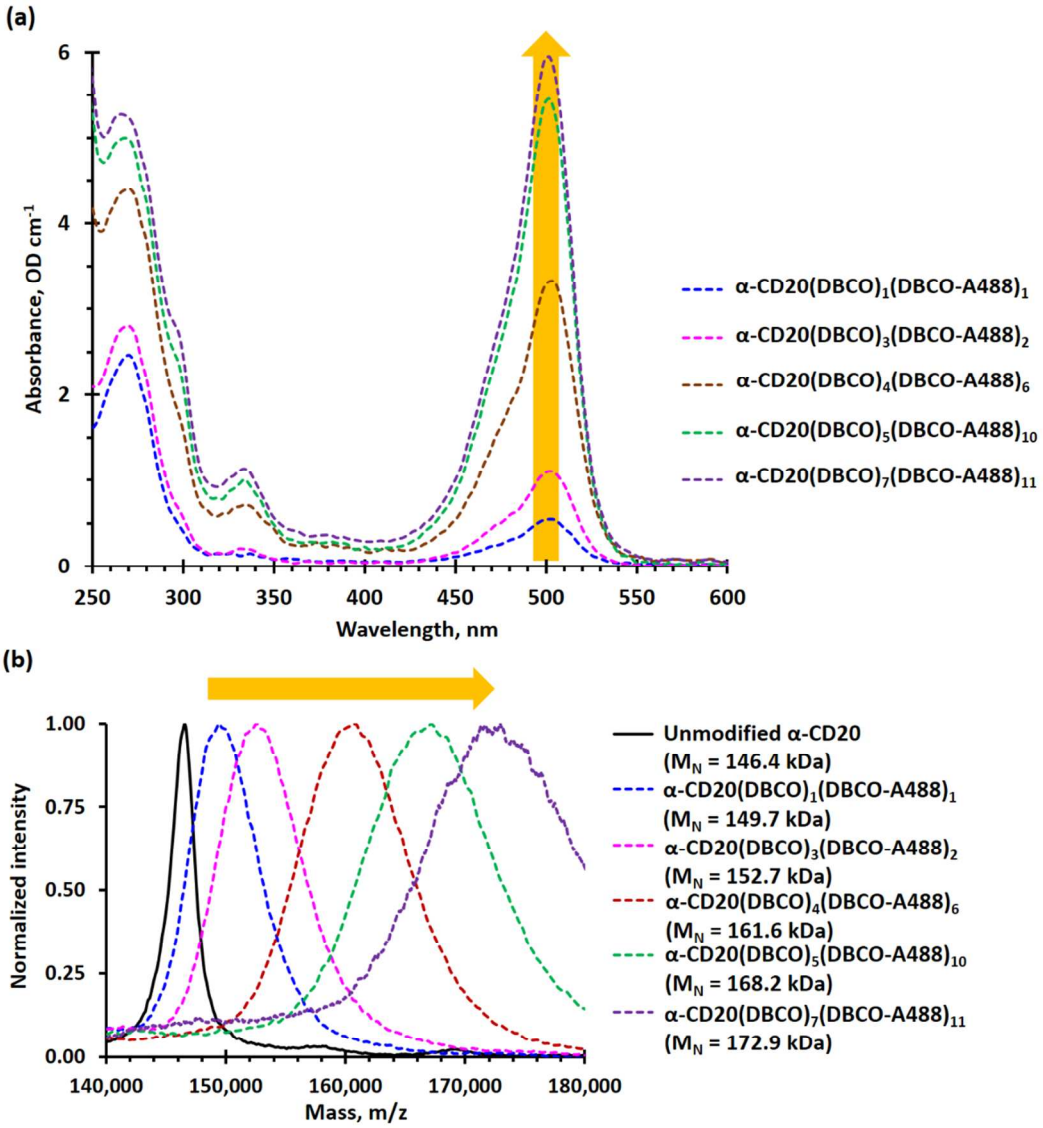

Figure S2. Characterization of Alexa Fluoro 488 (A488)-labeled α-CD20(DBCO)$_f$ for antibody-binding affinity study via FACS binding assay. The α-CD20 were functionalized through SPAAC between azide-functionalized A488 and terminal DBCO in the α-CD20(DBCO)$_f$. The target azide-to-DBCO ratio was 1:1. (a) UV-visible spectra of different A488-labeled α-CD20(DBCO)$_f$ (1 mg/mL, 6.95 μM). (b) MALDI-TOF mass spectra of different A488-labeled α-CD20(DBCO)$_f$.

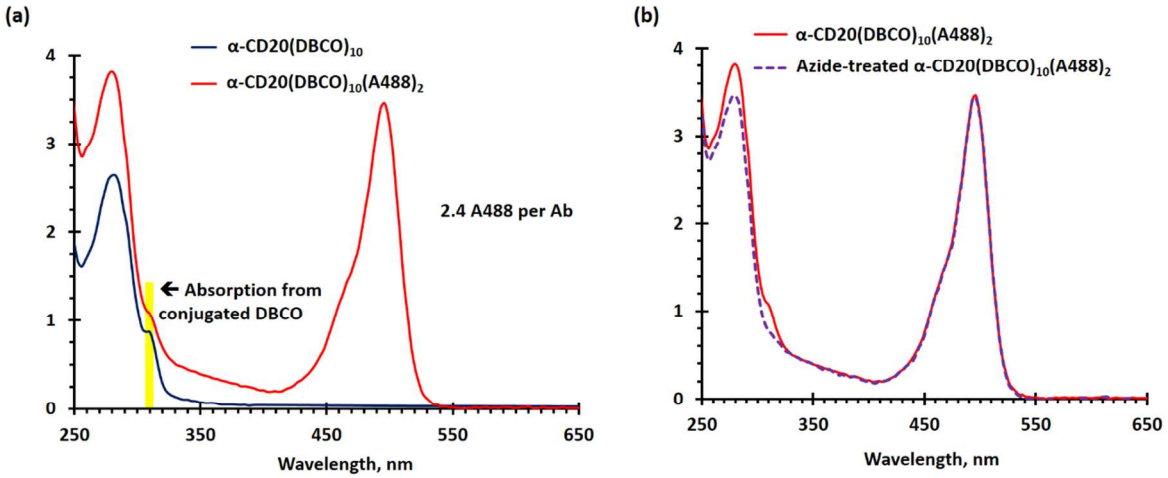

Figure S3. Characterization of A488-labeled α-CD20(DBCO)$_{10}$ for *in vitro* cell labeling and ex vivo biodistribution studies. (a) UV-visible absorption spectra of α-CD20(DBCO)$_{10}$ and α-CD20(DBCO)$_{10}$(A488)$_2$. The concentrations of both antibodies were 1 mg/mL (6.95 μM). A488 was conjugated to the antibody through amine-NHS ester coupling reaction. The target A488-to-α-CD20(DBCO)$_{10}$ molar ratio was 5:1. It was calculated that each antibody contained an average of 2 conjugated A488. (b) UV-visible absorption spectra of α-CD20(DBCO)$_{10}$(A488)$_2$ and "preblocked" α-CD20(DBCO)$_{10}$(A488)$_2$. The terminal DBCO was "preblocked" by the SPAAC with a large excess of NaN_3. The disappearance of the DBCO band at 310 nm confirmed the conversion of DBCO into triazole. The concentrations of both antibodies were 1 mg/mL (6.95 μM).

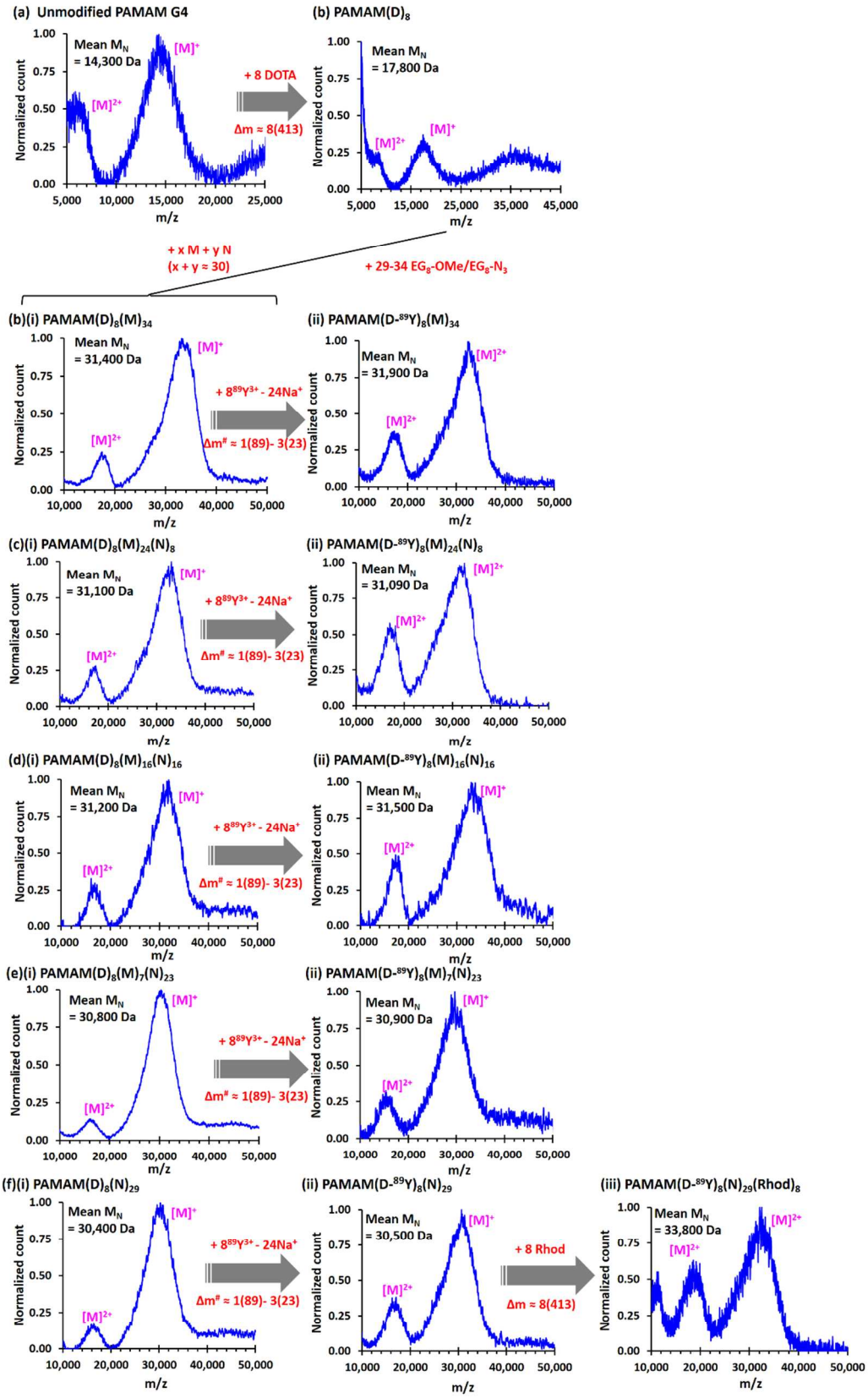

Figure S4. MALDI-ToF mass spectra of different dual-functionalized PAMAM.

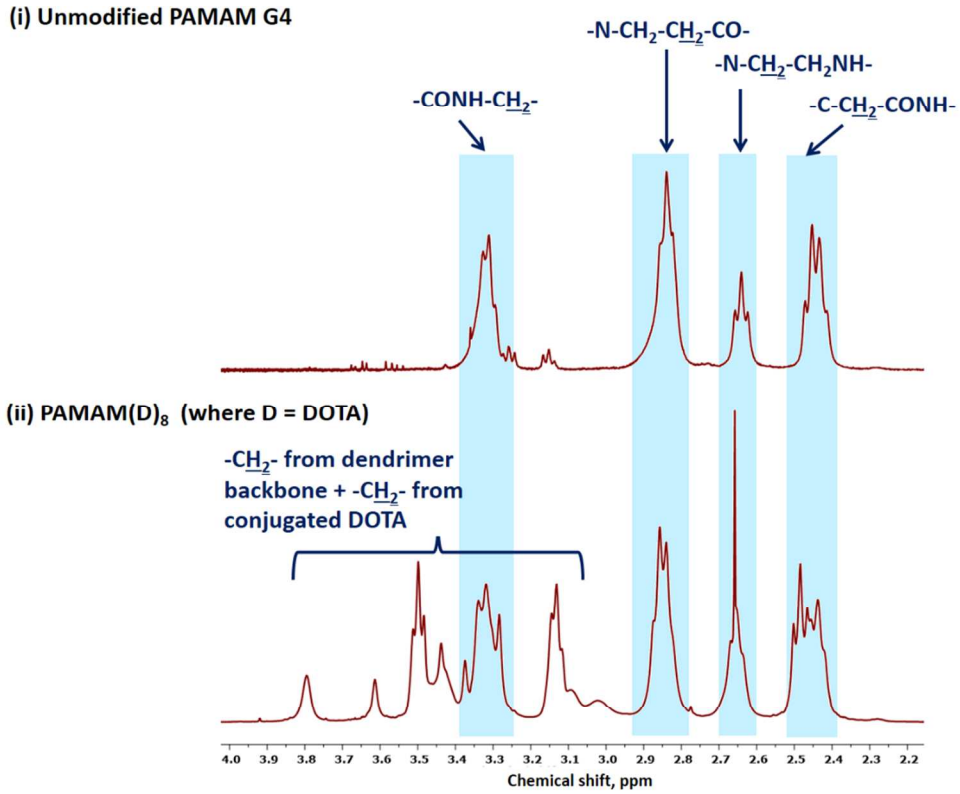

Figure S5. Assigned ^{1}H NMR spectra (400 MHz, D_2O, 293K, 1024 scans) of (i) unmodified PAMAM G4, and (ii) DOTA-functionalized PAMAM (denoted as PAMAM(D)$_8$). It is not possible to quantify the average number of conjugated DOTA from the ^{1}H NMR spectrum of PAMAM(D)$_8$ due to spectral overlap between the -C$\underline{H_2}$- protons in the dendrimer backbone and DOTA. The target EG$_8$-OMe to EG$_8$-$CH_2CH_2N_3$ molar ratios were (i) 1:0, (ii) 3:1, (iii) 1:1, (iv) 1:3, and (v) 0:1, respectively. The intensities of the singlet at 3.39 ppm that attributed to the terminal methoxyl protons from the conjugated -EG$_8$-OC$\underline{H_3}$ ligand decreased when the target -EG$_8$-OMe to -EG$_8$-$CH_2CH_2N_3$ molar ratios decreased. Due to spectral overlap, it is not possible to quantify the average number and molar ratios of -EG$_8$-OMe and -EG$_8$-$CH_2CH_2N_3$ from the ^{1}H NMR spectra.

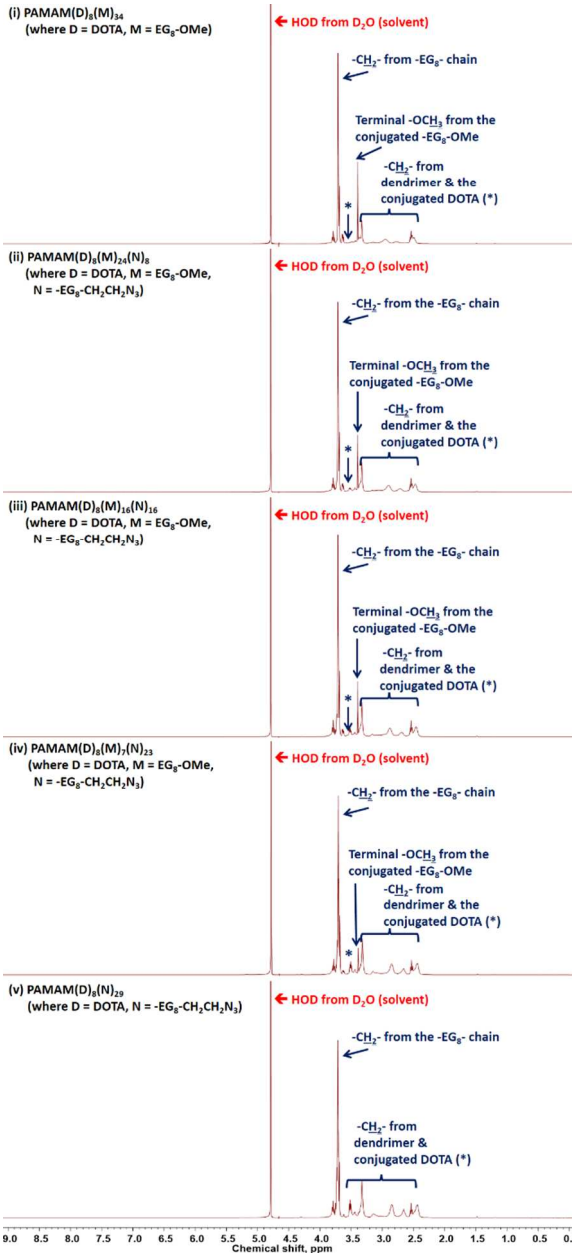

Figure S6. Assigned ^{1}H NMR spectra (D_2O, 400 MHz, 1024 scans) of DOTA and -EG_8-OMe and/or -EG_8-$CH_2CH_2N_3$ dual-functionalized PAMAM prepared from PAMAM(D)$_8$. The target -EG_8-OMe to -EG_8-$CH_2CH_2N_3$ molar ratios were (i) 1:0, (ii) 3:1, (iii) 1:1, (iv) 1:3, and (v) 0:1, respectively. The intensities of the singlet at 3.39 ppm that attributed to the terminal methoxyl protons from the conjugated -EG_8-O<u>CH$_3$</u> ligand decreased when the target -EG_8-OMe to -EG_8-$CH_2CH_2N_3$ molar ratios decreased. Due to spectral overlap, it is not possible to quantify the average number and molar ratios of -EG_8-OMe and -EG_8-$CH_2CH_2N_3$ from the ^{1}H NMR spectra.

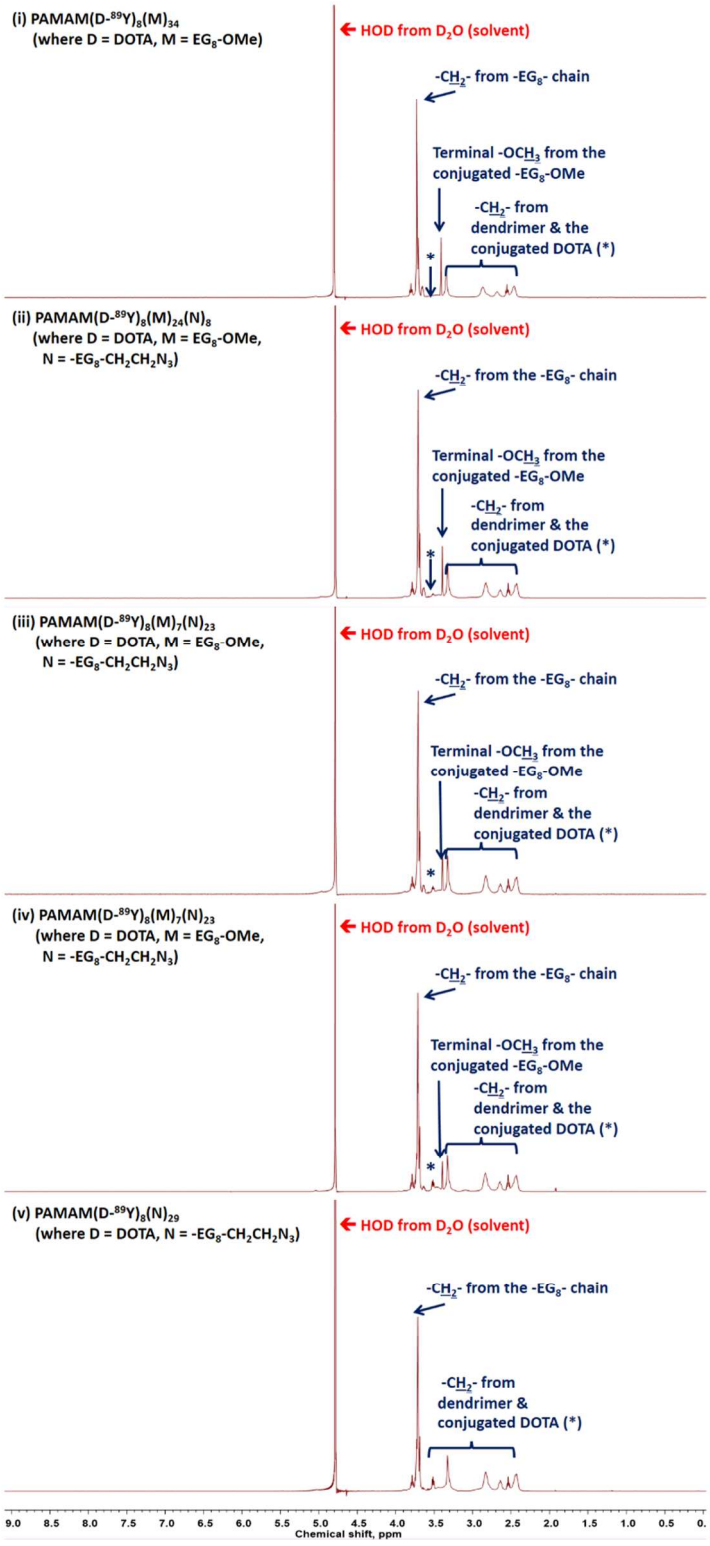

Figure S7. Assigned ^{1}H NMR spectra (D_2O, 400 MHz, 1024 scans) of non-radioactive yttrium-89 ($^{89}Y^{3+}$) -loaded dual-functionalized PAMAM. The ^{1}H NMR spectra of yttrium-89-loaded

dual-functionalized PAMAM are nearly identical to the spectra recorded before yttrium-89 loading.

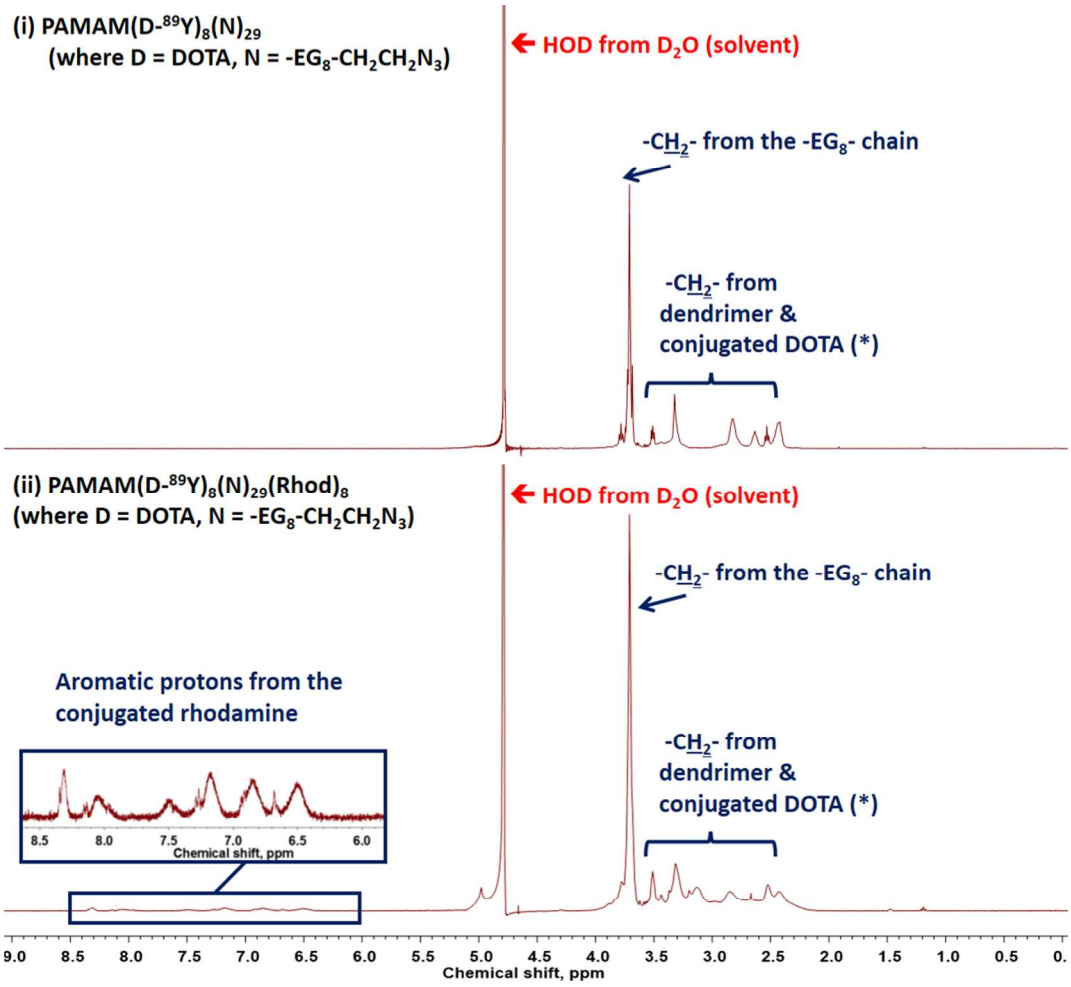

Figure S8. Assigned ^{1}H NMR spectra (D_2O, 400 MHz, 1024 scans) of yttrium-89-loaded DOTA and azide dual-functionalized PAMAM recorded (i) before and (ii) after labeling with rhodamine. The broad aromatic proton bands between 6.0 and 8.5 ppm can be attributed to the conjugated rhodamine.

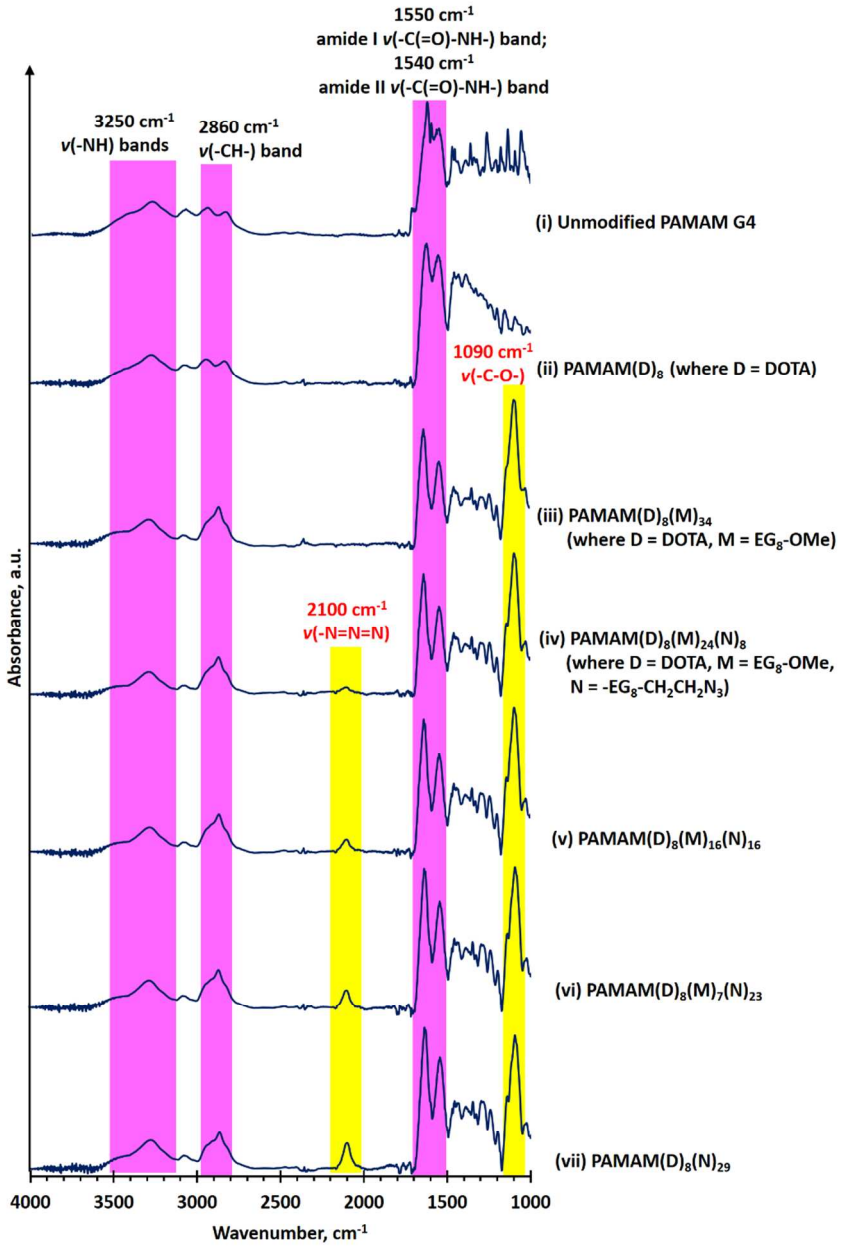

Figure S9. Assigned ATR FTIR spectra of (i) unmodified PAMAM G4, (ii) DOTA-functionalized PAMAM (denoted as PAMAM(D)$_8$), and (iii-vii) -EG$_8$-OMe and/or -EG$_8$-$CH_2CH_2N_3$ and DOTA dual-functionalized PAMAM G4 prepared from PAMAM(D)$_8$. The

target -EG_8-OMe to -EG_8-$CH_2CH_2N_3$ molar ratios were (iii) 1:0, (iv) 3:1, (v) 1:1, (vi) 1:3, and (vii) 0:1, respectively. The absorbance of the azide vibration band (ν(-N=N=N)) at 2100 cm^{-1} increased with the -EG_8-$CH_2CH_2N_3$ to -EG_8-OMe molar ratios due to the increased number of terminal azide groups.

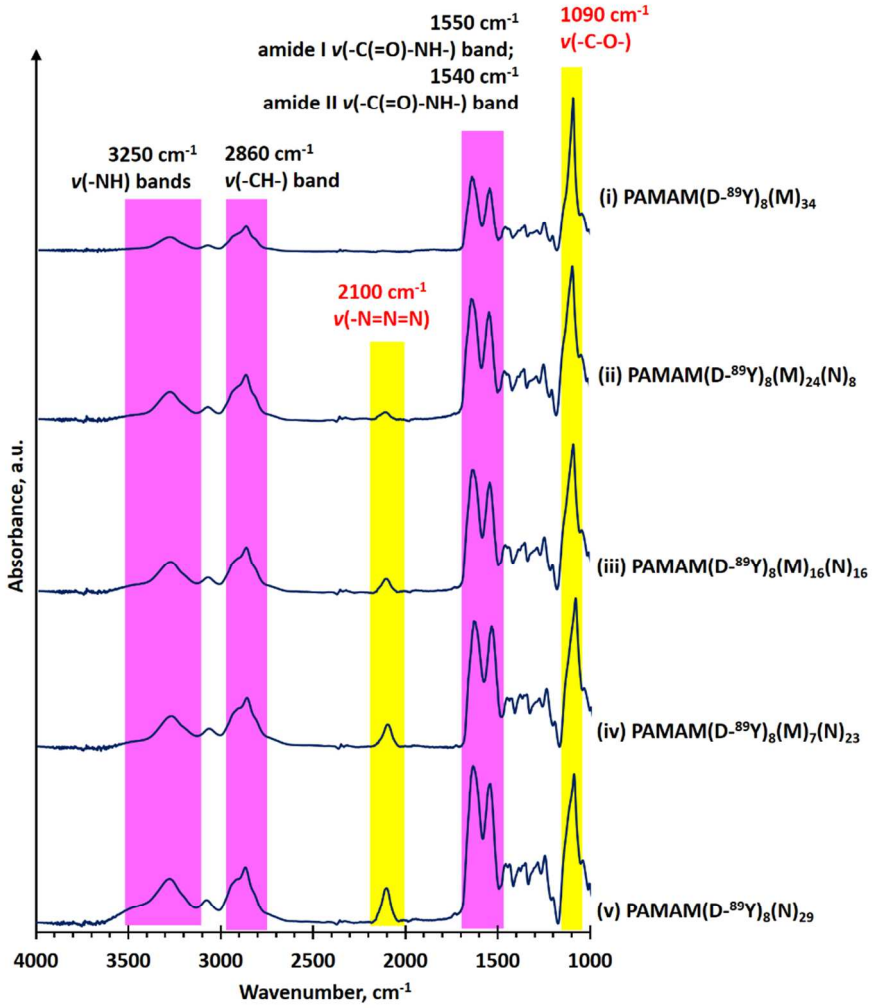

Figure S10. Assigned ATR FTIR spectra of yttrium-89-loaded dual-functionalized PAMAM G4. The absorbance of the azide vibration band (ν(-N=N=N) = 2100 cm^{-1}) of the yttrium-loaded dendrimers was comparable to that recorded before yttrium loading, which confirms that the moderate Y-89 loading conditions did not induce deazidation (*i.e.,* dissociation of terminal azide group).

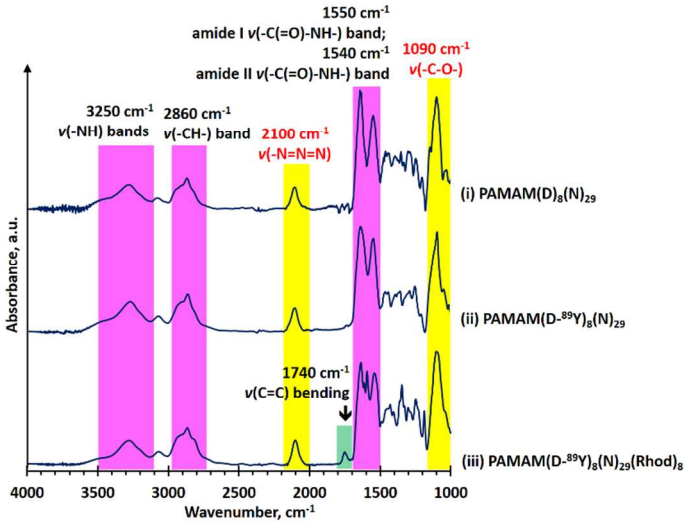

Figure S11. Assigned ATR FTIR spectra of (i) PAMAM(D)$_8$(M)$_{34}$, (ii) yttrium-loaded PAMAM(D-^{89}Y)$_8$(M)$_{34}$, and (iii) PAMAM(D-^{89}Y)$_8$(M)$_{34}$(Rhod)$_8$. The new vibration band at 1740 cm^{-1} of PAMAM(D-^{89}Y)$_8$(M)$_{34}$(Rhod)$_8$ can be attributed to ν(C=C) bending from the aromatic rings in the conjugated rhodamine.

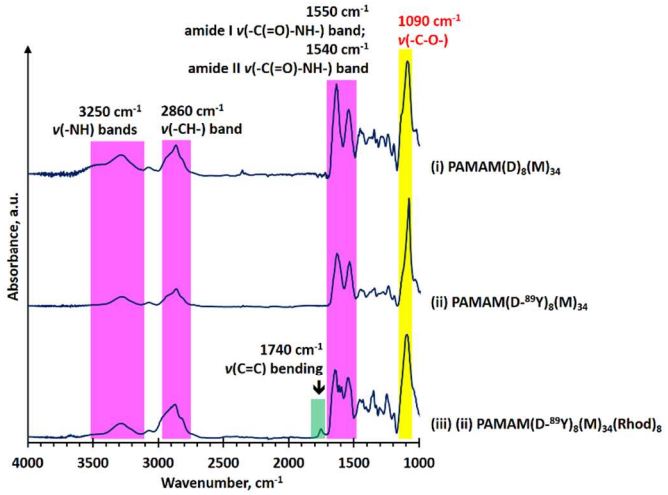

Figure S12. Assigned ATR FTIR spectra of (i) PAMAM(D)$_8$(N)$_{29}$, (ii) yttrium-loaded PAMAM(D-Y)$_8$(N)$_{29}$, and (iii) PAMAM(-^{89}Y)$_8$(N)$_{29}$(Rhod)$_8$. The new vibration band at 1740 cm^{-1} of PAMAM(D)$_8$(M)$_{34}$(Rhod)$_8$ can be attributed to ν(C=C) bending from the aromatic rings in the conjugated rhodamine. The absorbance of the azide vibration band (ν(-N=N=N) = 2100 cm^{-1}) of the rhodamine-labeled dendrimer is comparable to that recorded before rhodamine-conjugation, which confirms that the moderate rhodamine-labeling conditions did not induce deazidation (*i.e.,* dissociation of terminal azide group).

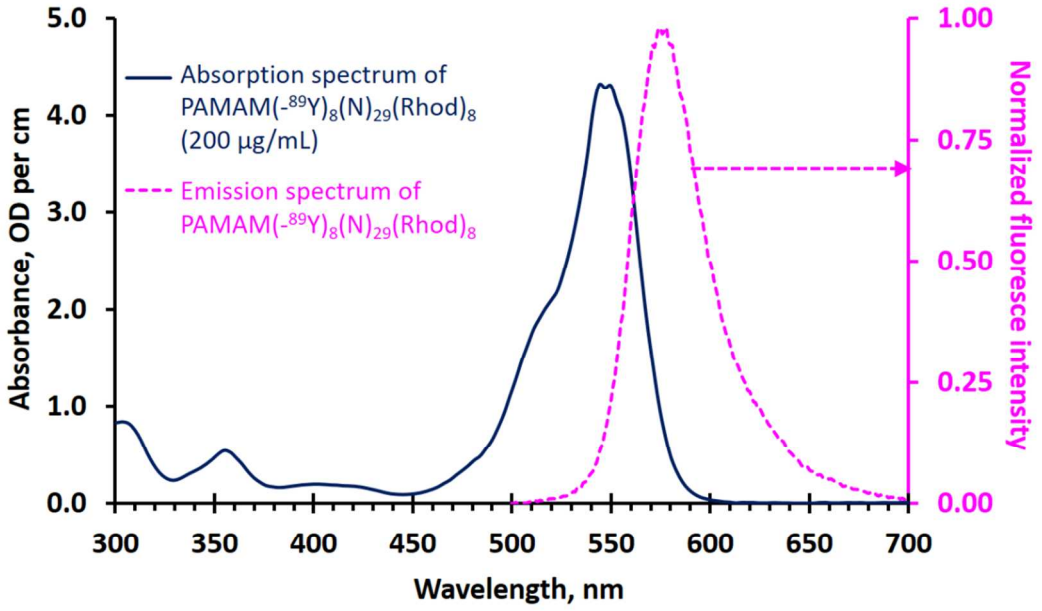

Figure S13. UV-visible absorption and emission spectra of PAMAM(D-^{89}Y)$_8$(N)$_{29}$(Rhod)$_8$. The emission spectrum of PAMAM(D-^{89}Y)$_8$(N)$_{29}$(Rhod)$_8$ was recorded using a light source excited at 480 ± 20 nm.

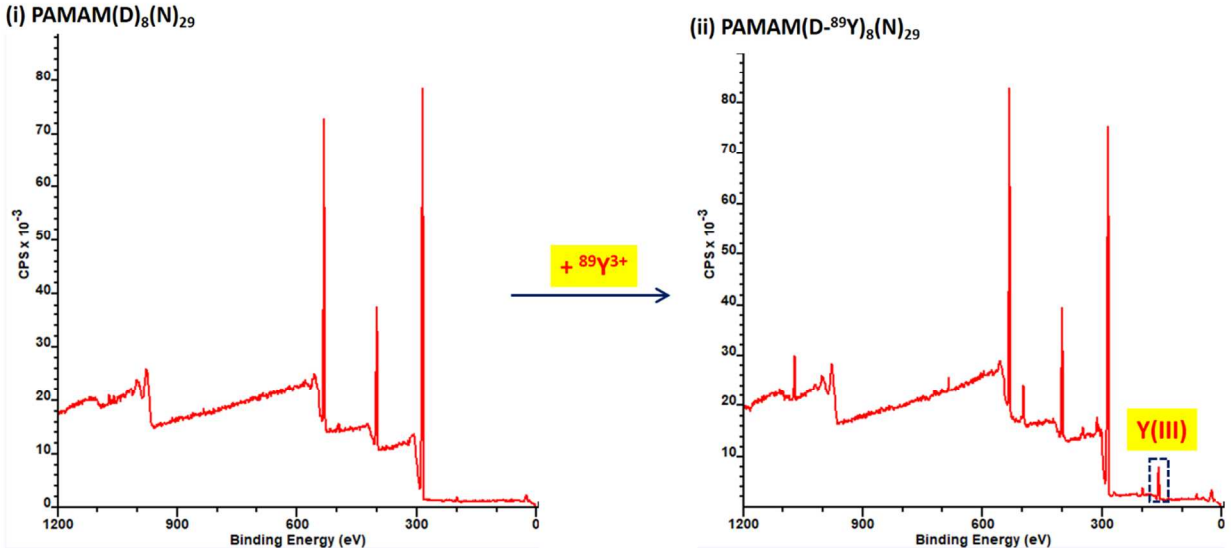

Figure S14. XPS spectra of (i) PAMAM(D)$_8$(N)$_{29}$ and (ii) PAMAM(D-^{89}Y)$_8$(N)$_{29}$. The sharp band at approximately 156 eV can be attributed to the coordinated Y(III).

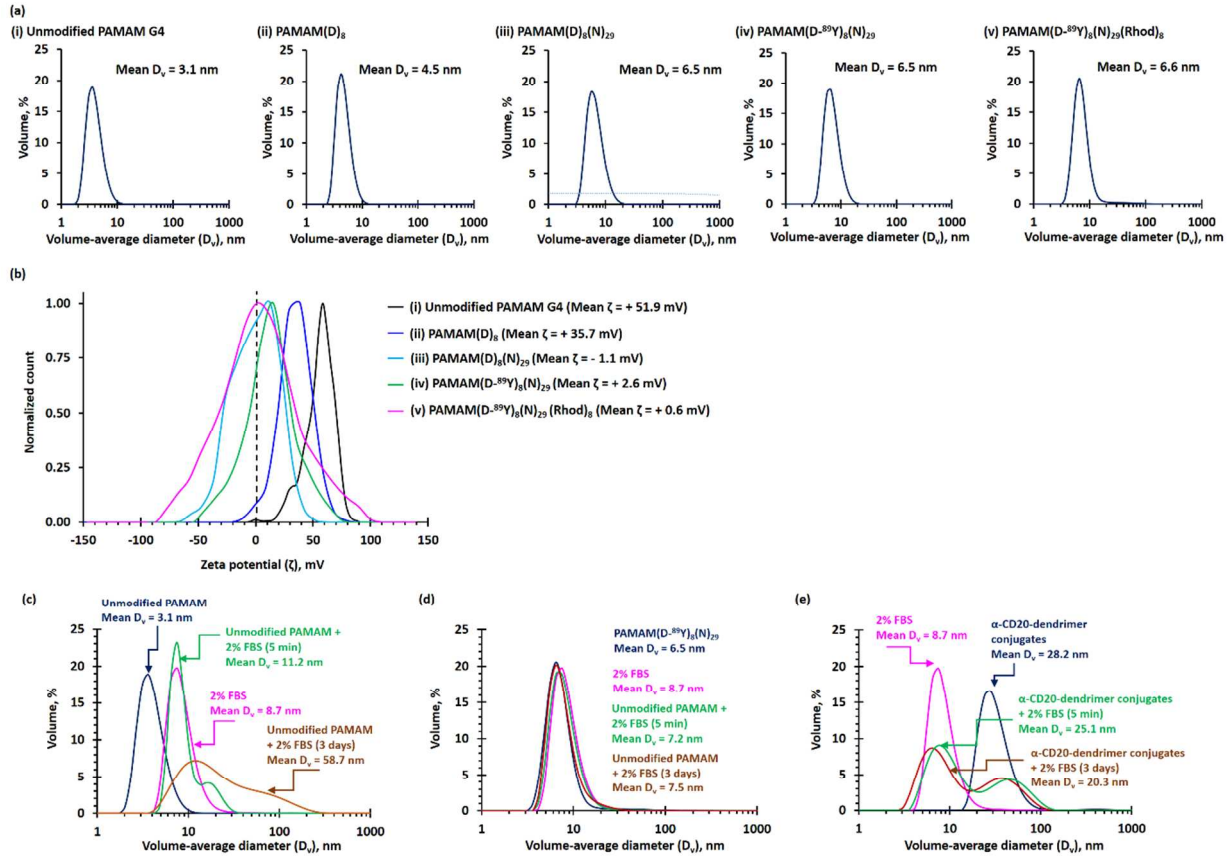

Figure S15. (a) Volume-average diameter (D_v) distribution curves and (b) zeta potential (ζ) distribution curves of (i) unmodified PAMAM G4, (ii) PAMAM(D)$_8$, (iii) PAMAM(D)$_8$(N)$_{29}$, (iv) PAMAM(D-^{89}Y)$_8$(N)$_{29}$, and (iv) PAMAM(D-^{89}Y)$_8$(N)$_{29}$(Rhod)$_8$, as determined by dynamic light scattering (DLS) and aqueous electrophoresis methods. All samples were dispersed in 0.1 M PBS (pH 7.4) prior to all measurements. The functionalization of cationic PAMAM G4 with non-ionic oligoethylene glycol effectively shielded the cationic charge from the cationic polyamine core. (c-d) The volume-average diameters (D_v) of (c) unmodified PAMAM G4, (d) PAMAM(D-^{89}Y)$_8$(N)$_{29}$ and (e) α-CD20-dendrimer premixtures recorded before, 5 min and 3 days after mixing with 2% FBS at the physiological conditions (1X PBS, 37 °C), as monitored by *ex situ* DLS method. PAMAM(D-^{89}Y)$_8$(N)$_{29}$ and α-CD20-dendrimer premixtures establish excellent stabilities in the physiological in the presence of 2% FBS (at 37 °C).

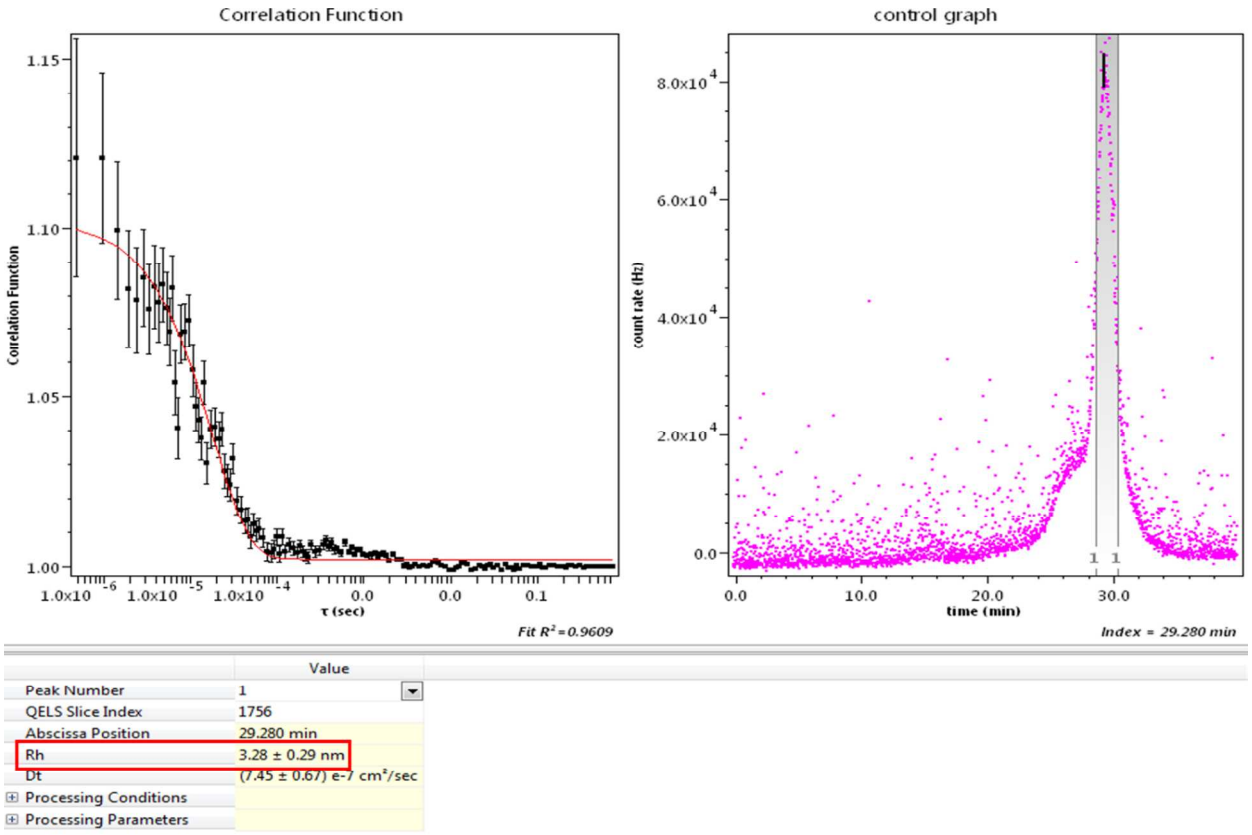

Figure S16. Size exclusion chromatography-differential refractometry (SEC-dRI) curve recorded for PAMAM(D-^{89}Y)$_8$(N)$_{29}$. The mean hydrodynamic diameter (mean D_h = 2 × mean hydrodynamic radius (mean R_h)) was found to be 6.6 nm.

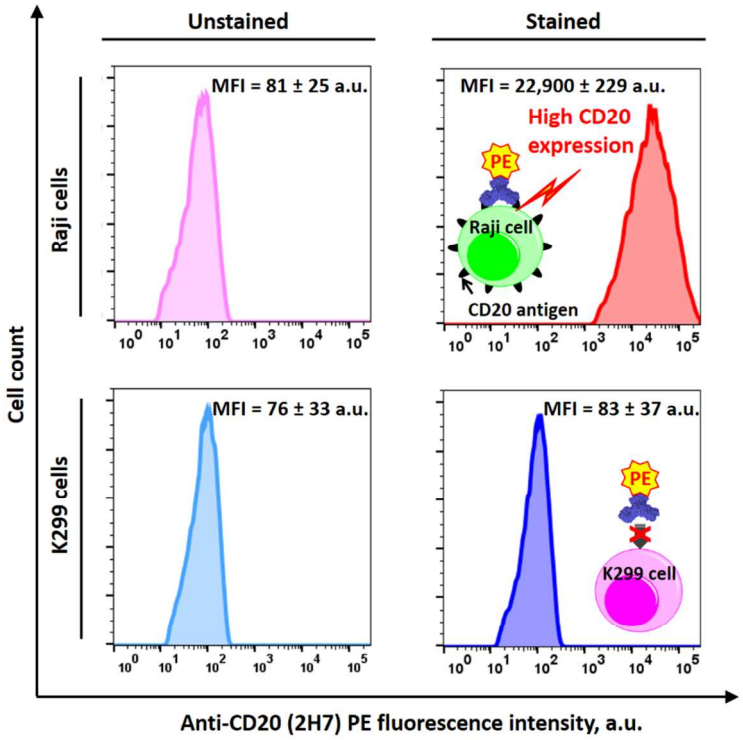

Figure S17. CD20 antigen expressions in Raji and K299 cell lines, as determined by flow cytometry using commercial-source PE-labeled anti-human CD20 antibody. Raji overexpress CD20 antigen (i.e., $CD20^{+}$). The CD20 antigen expression in K299 cells is very low (*i.e.,* $CD20^{-}$).

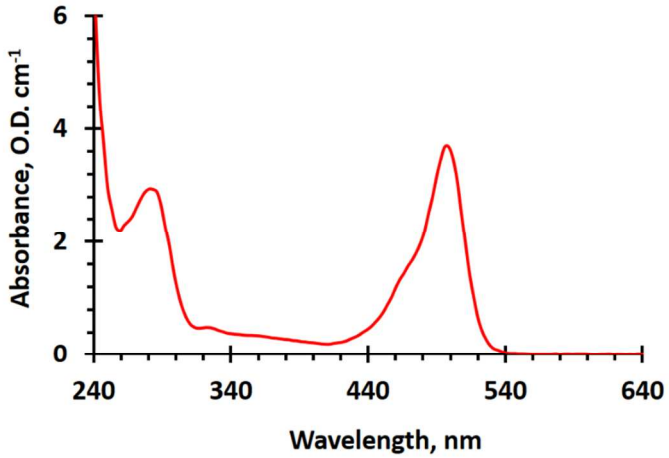

Figure S18. UV-visible absorption spectrum of FITC-labeled Rituximab. It was calculated that each antibody contained an average of 8 conjugated FITC.

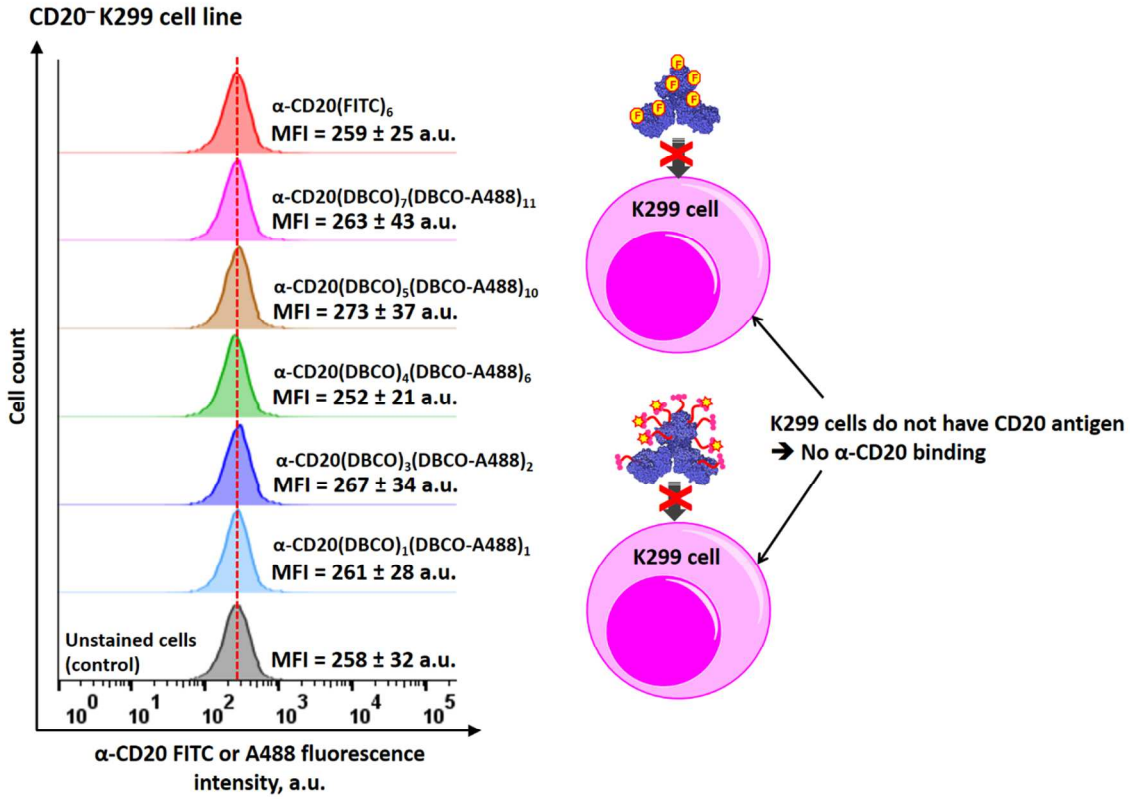

Figure S19. Representative flow cytometry histograms of CD20-negative K299 cells after staining with 97.11 nM of different dye-labeled α-CD20. No binding could be observed under the experimental conditions due to the absence of CD20 antigen in the K299 cells.

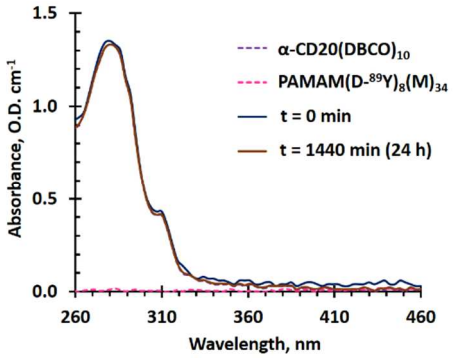

Figure S20. UV absorption spectra of α-CD20(DBCO)$_{10}$ (3.13 μM, final concentration) after incubation with azide-free PAMAM(D-^{89}Y)(M)$_{34}$ (3.13 μM, final concentration) at 37 °C for up

to 24 h. Due to the absence of terminal azide, the absorbance at 280 nm and 310 nm in the α-CD20(DBCO)$_{10}$ remained unchanged at the physiological conditions.

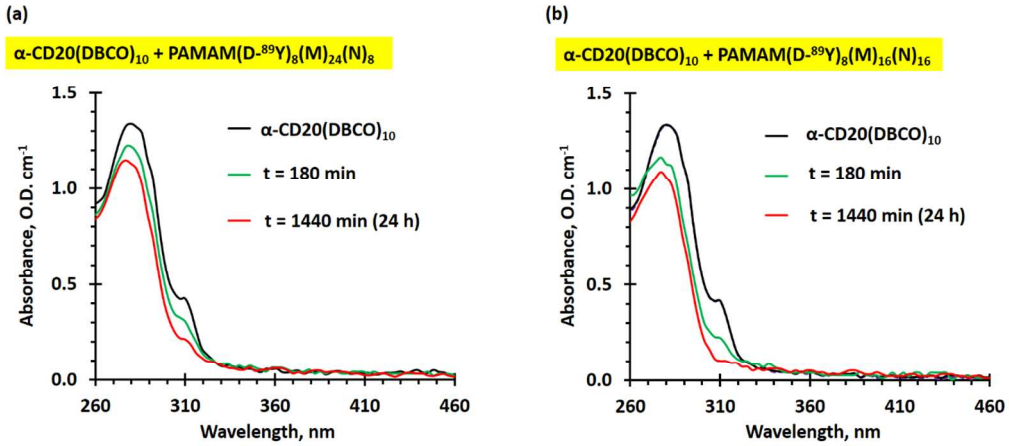

Figure S21. UV absorption spectra of α-CD20(DBCO)$_{10}$ (3.13 μM, final concentration) after incubated with (a) PAMAM(D-^{89}Y)(M)$_{24}$(N)$_8$ and (b) PAMAM(D-^{89}Y)(M)$_{18}$(N)$_{18}$ (3.13 μM, final concentration) at 37 °C for 24 h.

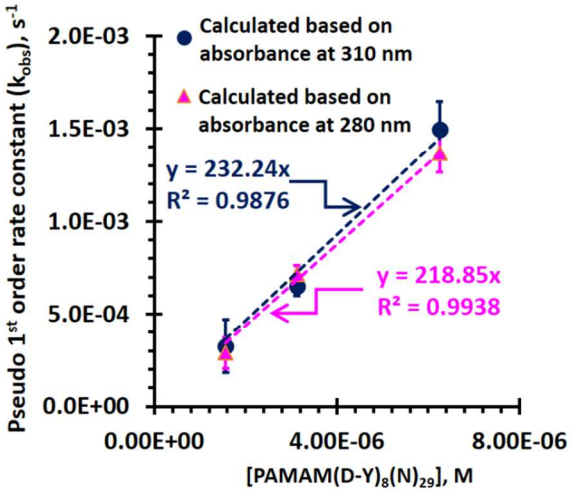

Figure S22. The plot of pseudo first-order rate constant of different bioorthogonal reaction pairs (obtained from the kinetics curves) versus the concentrations of PAMAM(D-^{89}Y)(N)$_{29}$. The concentration-dependent second-order rate constant of α-CD20(DBCO)$_{10}$ and PAMAM(D-^{89}Y)(N)$_{29}$ was calculated to be 232 M^{-1} s^{-1} (gradient of the curve).

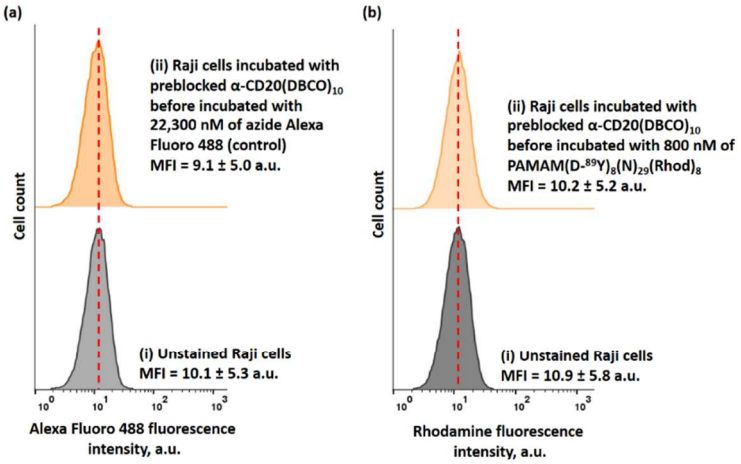

Figure S23. (a) Flow cytometry histograms of (i) unstained Raji cells, and (ii) Raji cells pretreated with pre-blocked α-CD20(DBCO)$_{10}$ before being stained with azide-A488. (b) Flow cytometry histograms of (i) unstained Raji cells, and (ii) Raji cells pretreated with pre-blocked α-CD20(DBCO)$_{10}$ before stained with PAMAM(D-^{89}Y)(N)$_{29}$(Rhod)$_8$. In both studies, DBCO in α-CD20 was pre-blocked by treatment with a large excess of NaN_3 before the binding study.

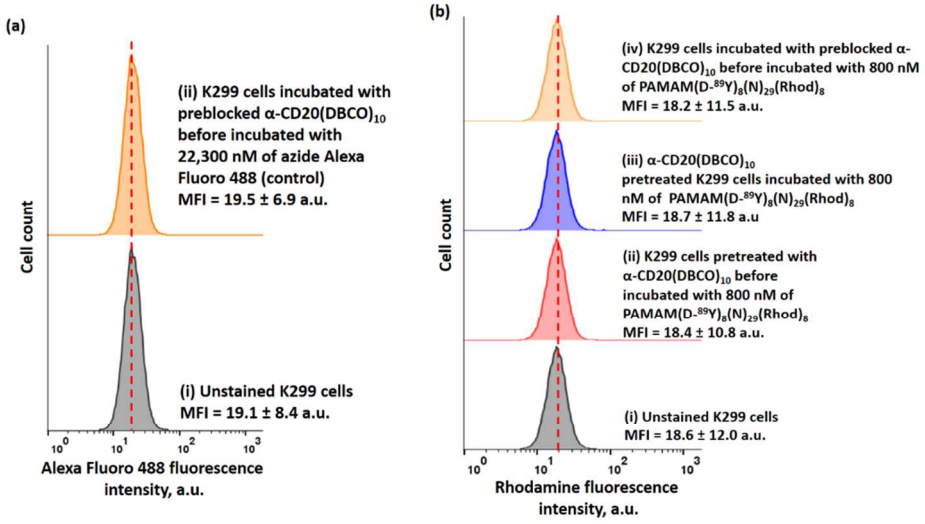

Figure S24. (a) Flow cytometry histograms of (i) unstained K299 cells, and (ii) K299 cells pretreated with α-CD20(DBCO)$_{10}$ before staining with azide-A488. (b) Flow cytometry histograms of (i) unstained K299 cells, (ii) K299 cells pretreated with α-CD20(DBCO)$_{10}$ before

staining with PAMAM(D-^{89}Y)$(N)_{29}(Rhod)_8$, (iii) K299 cells stained with antibody-dendrimer premixture, and (iv) K299 cells pretreated with pre-blocked α-CD20$(DBCO)_{10}$ before staining with PAMAM(D-^{89}Y)$(N)_{29}(Rhod)_8$. No non-specific cell labeling could be observed due to the absence of CD20 antigen in the K299 cells.

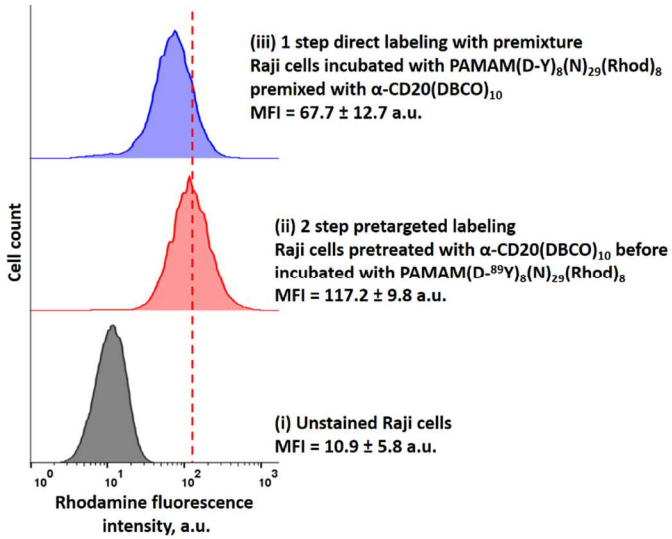

Figure S25. Flow cytometry histograms of (i) unstained Raji cells, (ii) Raji cells strained using a 2-step pretargeted labeling method (i.e., cells first treated with α-CD20$(DBCO)_{10}$, washed, then stained with PAMAM(D-^{89}Y)$(N)_{29}(Rhod)_8$), and (iii) Raji cells directly stained with antibody-dendrimer premixture. The concentration of Rhod-labeled PAMAM in all 3 cases were 800 nM.

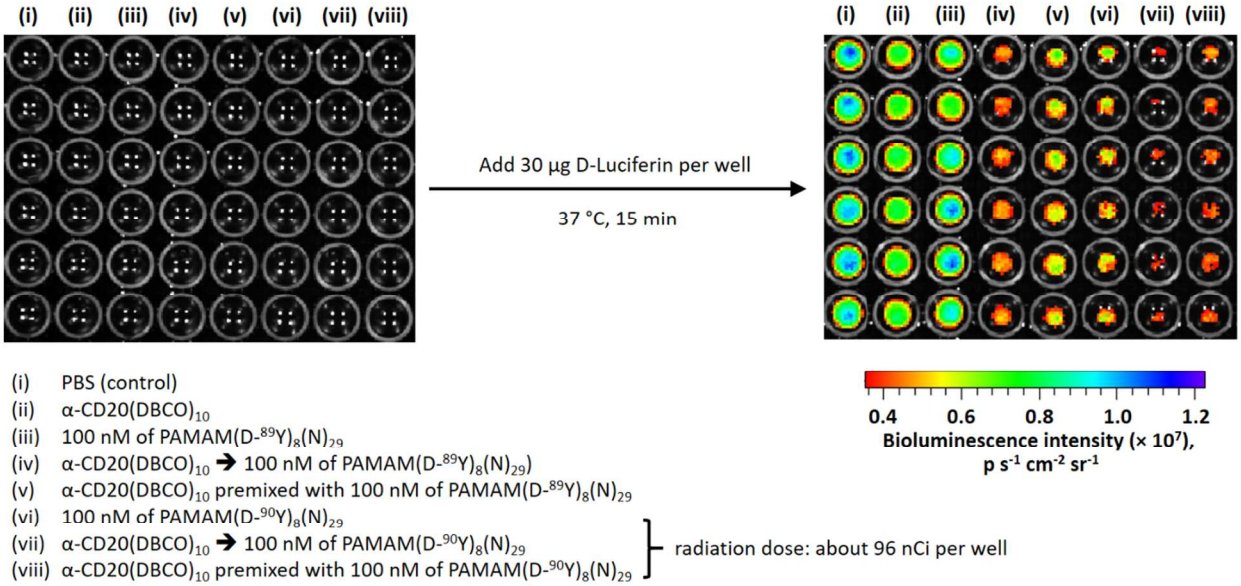

Figure S26. Bioluminescence images of different antibody- and/or dendrimer-treated Raji-Luc cells recorded before and after the addition of D-luciferin to the cells. Insignificant amount of Cherenkov radiation were detected in cells treated with Y-90-labeled PAMAM (wells (vi) - (viii)).

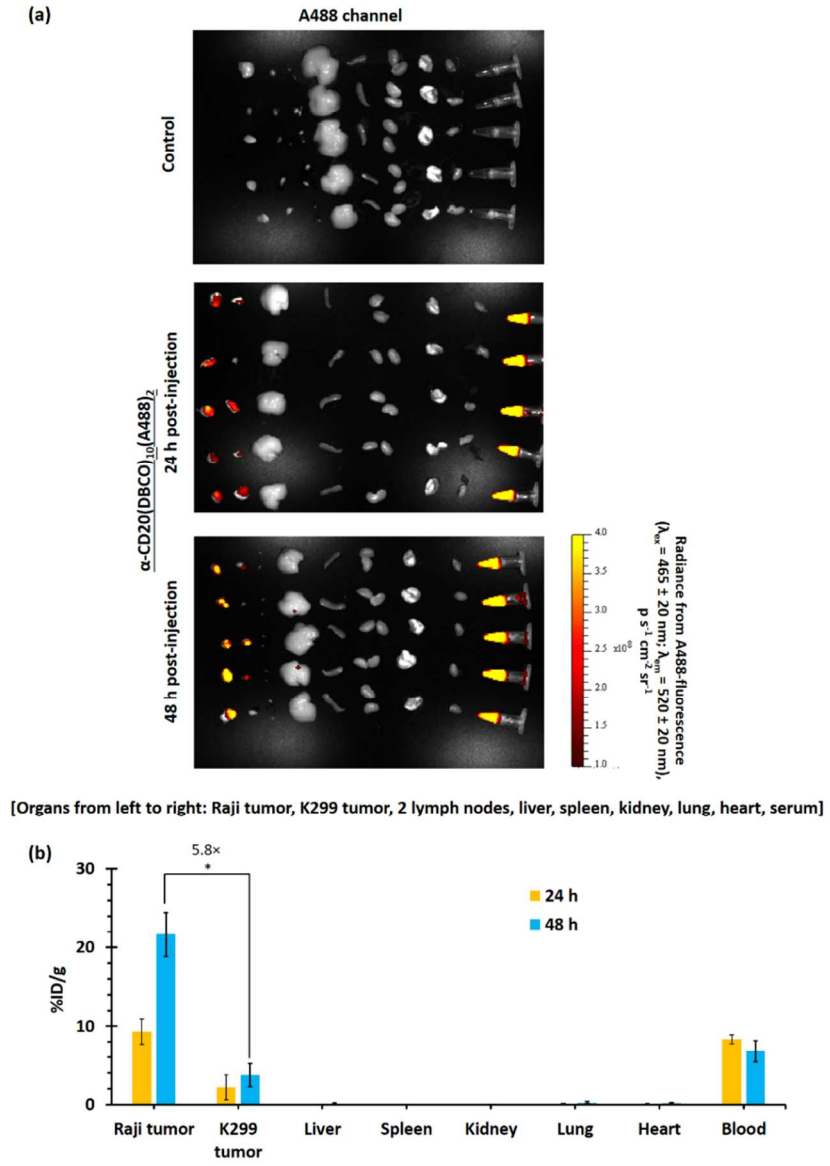

Figure S27. Biodistribution of α-CD20(DBCO)$_{10}$(A488)$_2$ in dual-xenograft tumor-bearing mice. (a) *Ex vivo* fluorescence images of Raji xenograft tumor, CD20$^-$ K299 xenograft tumor, lymph nodes, liver, spleen, kidney, lung, heart, and plasma collected from the dual-xenograft tumor-

bearing mice 24 or 48 h after tail-vein i.v. administration of α-CD20(DBCO)$_{10}$(A488)$_2$ (or mice did not receive any treatment) recorded *via* A488 channel setting. (b) Biodistribution of α-CD20(DBCO)$_{10}$(A488)$_2$ in major organs determined from the *ex vivo* fluorescence images recorded using the A488 channel setting. (N.B. An insignificant amount of antibody (*i.e.,* < 1 %ID/g) was accumulated in the lymph nodes 48 h after i.v. administration of antibody. n = 5, * denotes $p < 0.05$.)

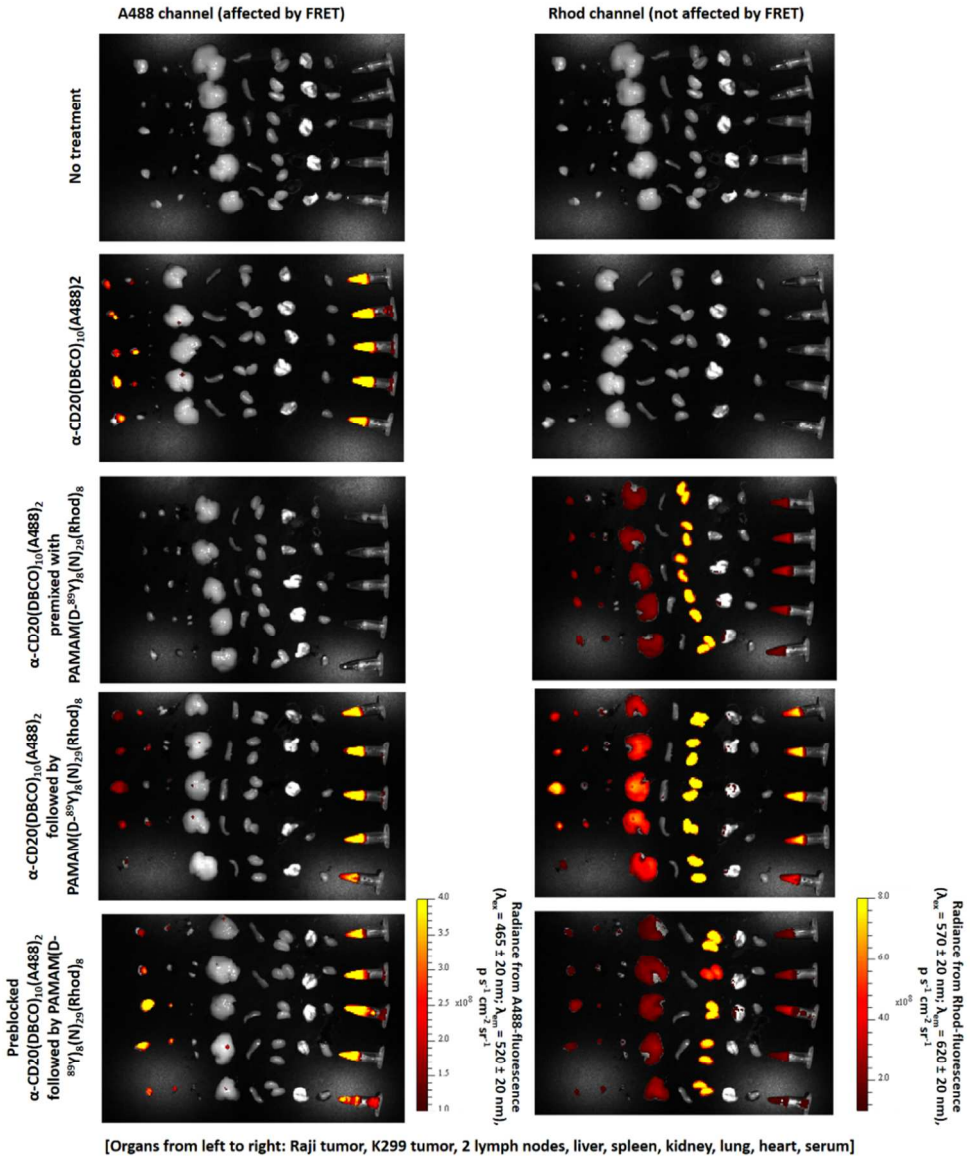

Figure S28. Biodistribution of PAMAM(D-^{89}Y)$_8$(N)$_{29}$(Rhod)$_8$ upon systemic administration of α-CD20(DBCO)$_{10}$(A488)$_2$ (or azide-pretreated α-CD20(DBCO)$_{10}$(A488)$_2$) in dual-xenograft tumor-bearing mice. *Ex vivo* fluorescence images of Raji xenograft tumor, K299 xenograft tumor, lymph nodes, liver, spleen, kidney, lung, heart, and plasma collected from mice that (i)

received no treatment (control), (ii) were treated with α-CD20(DBCO)$_{10}$(A488)$_2$ (6 mg/kg), (iii) were treated with α-CD20(DBCO)$_{10}$(A488)$_2$ (6 mg/kg) for 24 h before i.v. administration of PAMAM(D-^{89}Y)$_8$(N)$_{29}$(Rhod)$_8$ (20 mg/kg), (iv) received single i.v. administration of dendrimer-antibody premixture (containing 6 mg/kg of α-CD20(DBCO)$_{10}$(A488)$_2$ and 20 mg/kg of PAMAM(D-^{89}Y)$_8$(N)$_{29}$(Rhod)$_8$), and (v) were treated with preblocked α-CD20(DBCO)$_{10}$(A488)$_2$ (antibody incubated with PBS containing 0.1 wt% sodium azide at 20 °C for 1 h, then kept at 4 °C for 24 h prior to the study) for 24 h before i.v. administration of PAMAM(D-^{89}Y)$_8$(N)$_{29}$(Rhod)$_8$ (20 mg/kg).

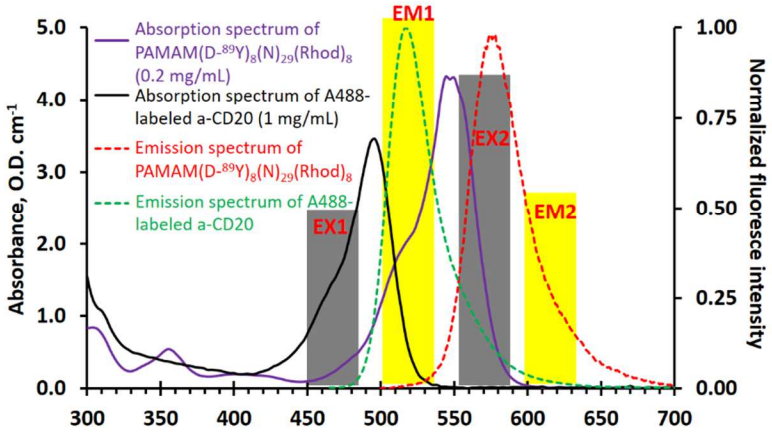

Figure S29. UV-visible absorption spectra and normalized fluorescent (emission) spectra of α-CD20(DBCO)$_{10}$(A488)$_2$ (1 mg/mL) and rhodamine-labeled dendrimer PAMAM(D-^{89}Y)$_8$(N)$_{29}$(Rhod)$_8$ (200 μg/mL). The fluorescent spectra of α-CD20(DBCO)$_{10}$(A488)$_2$ and PAMAM(D-^{89}Y)$_8$(N)$_{29}$(Rhod)$_8$ were recorded upon excitation at 450 and 480 nm, respectively. The grey highlighted regions represent the wavelength ranges of the excitation filters in the IVIS Kinetic preclinical optical imaging system selected for the excitation of A488 dye (denoted as "EX1") and rhodamine dye (denoted as "EX2"). The yellow highlighted regions represent the wavelength ranges of the emission filters in the IVIS Kinetic preclinical optical imaging system selected for the observation of fluorescence from the excited A488 dye (denoted as "EM1") and rhodamine dye (denoted as "EM2").

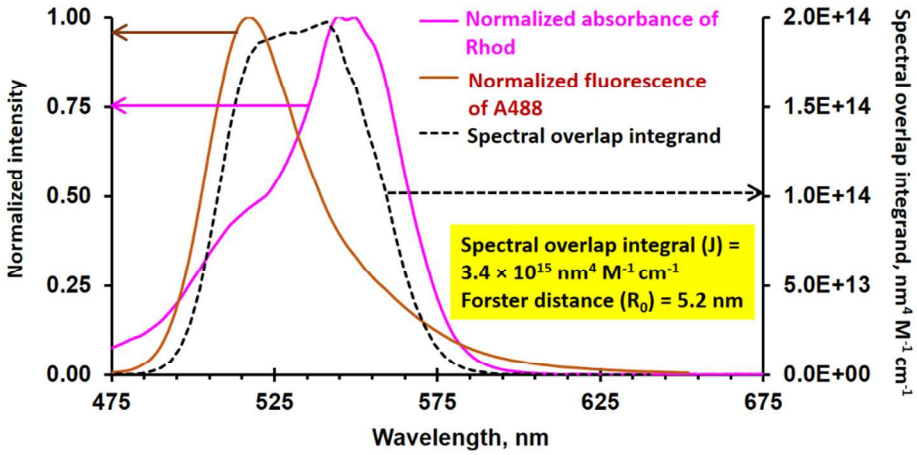

Figure S30. Normalized fluorescent (emission) spectrum of α-CD20$(DBCO)_{10}(A488)_2$ (brown curve), UV-visible absorption spectrum PAMAM$(D)_8(N)_{29}(Rhod)_8$ (pink curve), and the spectral overlap integral (black dotted line). The cumulative spectral integral (J) was calculated to be 3.4 × 10^{14} nm^4 M^{-1} cm^{-1}, and the Forster distance (R_0) was calculated to be 5.2 nm.

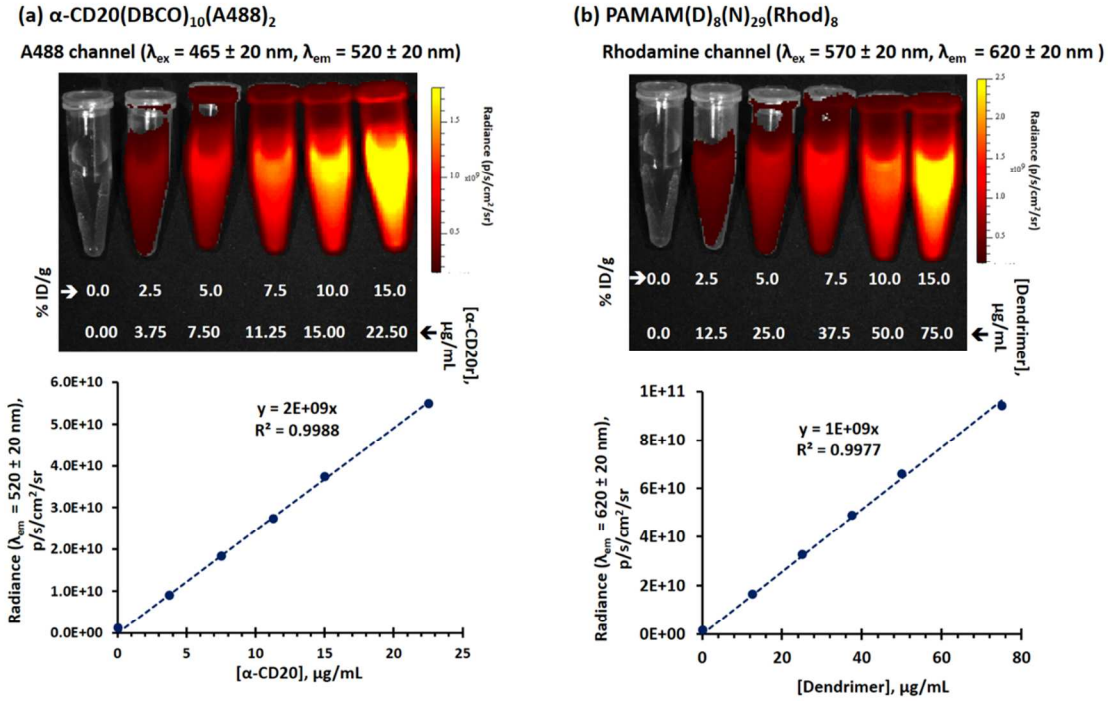

Figure S31. Fluorescence images of standard α-CD20$(DBCO)_{10}(A488)_2$ and PAMAM$(D\text{-}^{89}Y)_8(N)_{29}(Rhod)_8$ samples recorded using an IVIS Kinetic preclinical imaging system. (a) Fluorescence image of PBS (control), and 3.75 to 22.50 µg/mL of α-CD20$(DBCO)_{10}(A488)_2$ recorded with an excitation bandpass filter at 465 ± 20 nm and an emission band pass filter at 520 ± 20 nm ("A488 channel"). The concentrations of the standard antibody samples were

equivalent to 2.5 to 15.0 %ID/g of antibodies used in the *in vivo* imaging study. The radiances of the antibody samples increased linearly with the antibody concentrations up to 25 μg/mL. (b) Fluorescence images of PBS (control), and 12.5 – 75.0 μg/mL of PAMAM(D-^{89}Y)$_8$(N)$_{29}$(Rhod)$_8$ recorded with an excitation band pass filter at 570 ± 20 nm and an emission band pass filter at 620 ± 20 nm ("Rhod channel"). The concentrations of the standard antibody samples were equivalent to 2.5 to 15.0 %ID/g of dendrimer used in the *in vivo* imaging study. The radiances of dendrimer samples increased linearly with the antibody concentrations up to 80 μg/mL. Thus, the measured radiance can be used to quantify the concentrations of α-CD20(DBCO)$_{10}$(A488)$_2$ and PAMAM(D-^{89})$_8$(N)$_{29}$(Rhod)$_8$ in *ex vivo* samples.

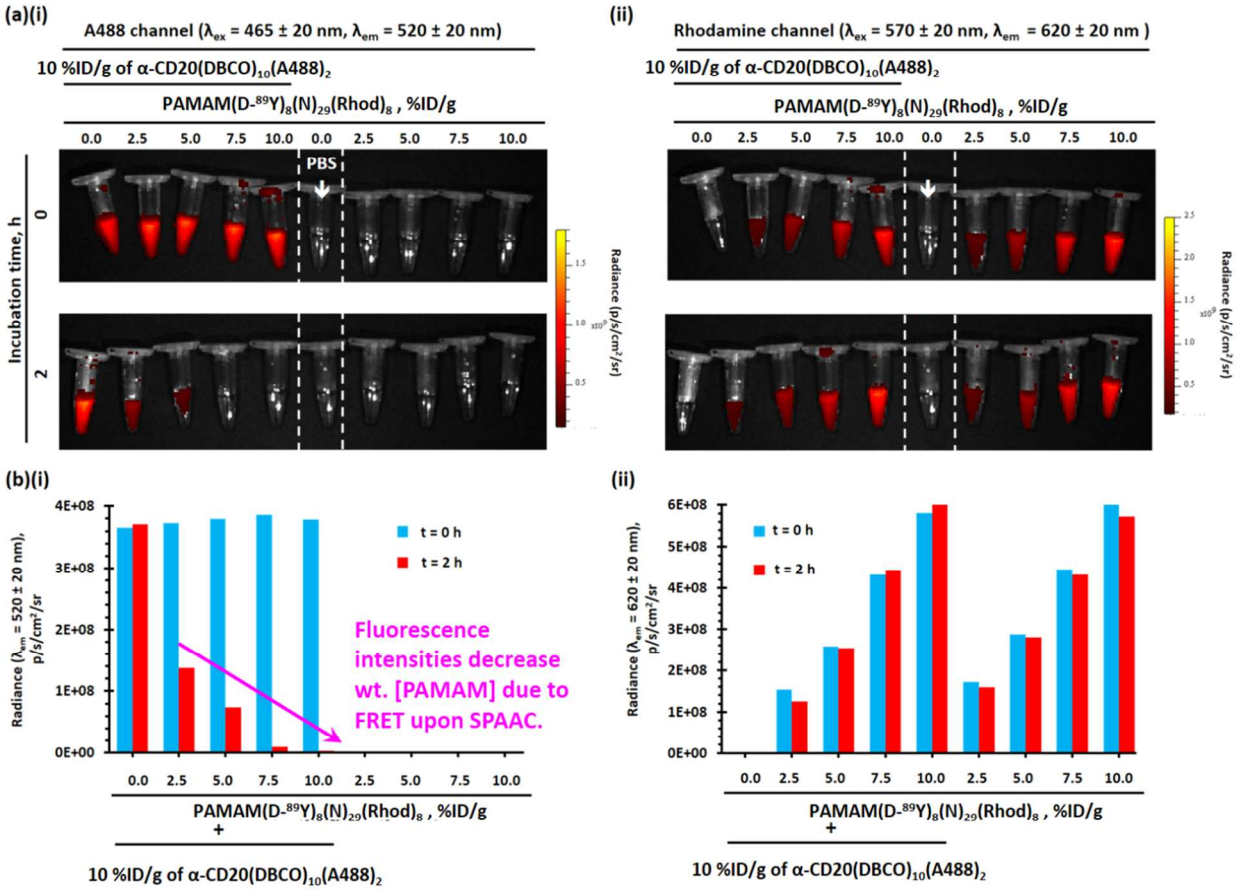

Figure S32. Observing FRET after PAMAM(D-^{89}Y)$_8$(N)$_{29}$(Rhod)$_8$ crosslinked with α-CD20(DBCO)$_{10}$(A488)$_2$ through an IVIS Kinetic preclinical imaging system. (a) Fluorescence images of 12.5 – 50.0 μg/mL of PAMAM(D-^{89}Y)$_8$(N)$_{29}$(Rhod)$_8$ (equivalent to 2.5 to 10.0 %ID/g of the dendrimer used in the *in vivo* imaging study) and PBS recorded immediately (< 1 min) and 2 h after mixing with 15 μg/mL of α-CD20(DBCO)$_{10}$(A488)$_2$ (equivalent to 10 % ID/g of α-CD20 used in the *in vivo* imaging study) through the (i) A488, and (ii) Rhod channels. The fluorescence intensities (recorded at the Rhod channel) of 15 μg/mL of α-CD20(DBCO)$_{10}$(A488)$_2$ dose-dependently decreased after incubation with 12.5 – 50.0 μg/mL of PAMAM(D-^{89}Y)$_8$(N)$_{29}$(Rhod)$_8$ at 37 °C for 2 h, whereas the fluorescence intensities recorded at the "Rhod channel" remained nearly constant. (b) Radiances of PBS and 12.5 – 50.0 μg/mL of PAMAM(D-^{89}Y)$_8$(N)$_{29}$(Rhod)$_8$ after mixing with 15 μg/mL of α-CD20(DBCO)$_{10}$(A488)$_2$.

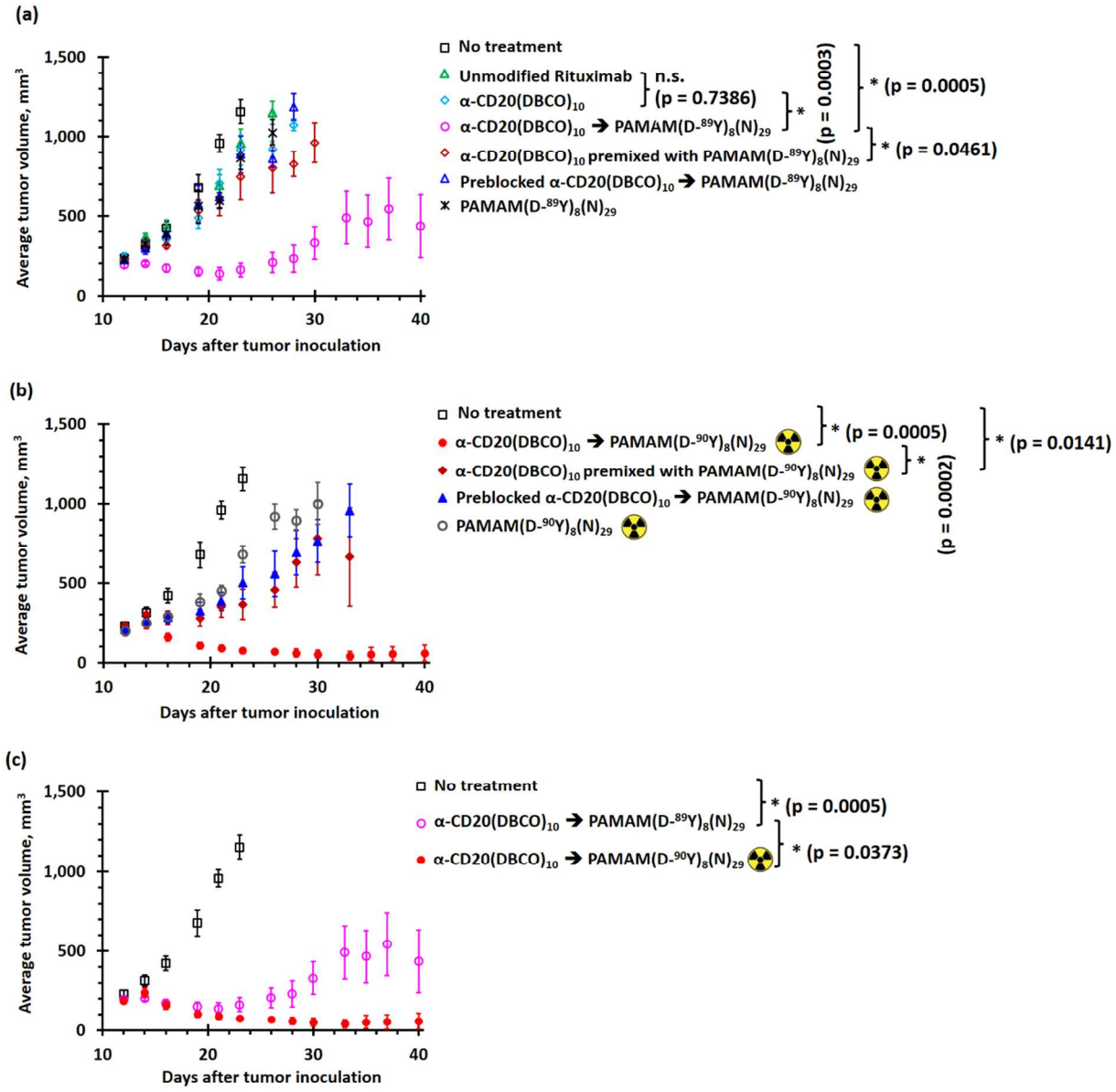

Figure S33. *In vivo* anticancer study in Raji xenograft tumor-bearing mice. (a) Average xenograft tumor volumes after treatment with α-CD20 (7.5 mg/kg) and/or non-radioactive PAMAM(D-^{89}Y)$_8$(N)$_{29}$ (25 mg/kg). (b) Average xenograft tumor volumes after treatment with α-CD20 (7.5 mg/kg) and/or radioactive PAMAM(D-^{90}Y)$_8$(N)$_{29}$ (25 mg/kg, 7.5 mCi/kg). (c) A comparison of average xenograft tumor volumes after pretargeted immunotherapy and pretargeted radioimmunotherapy.

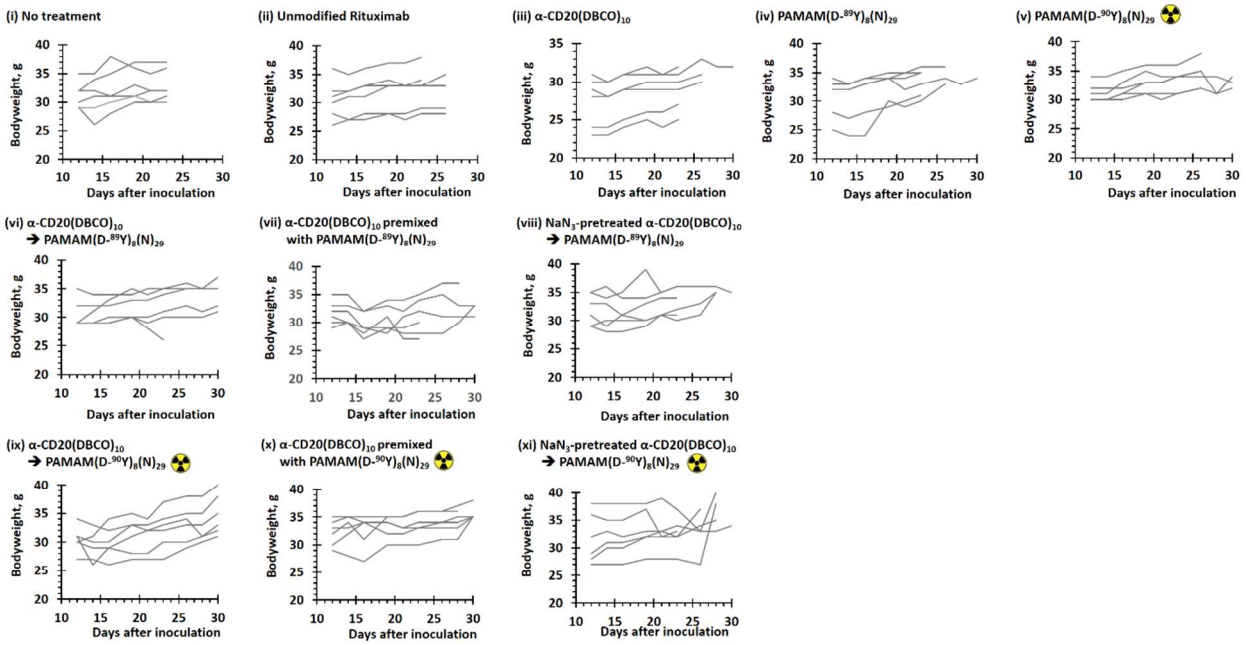

Figure S34. Bodyweight measurements of individual Raji xenograft tumor-bearing mice recorded after different treatments.

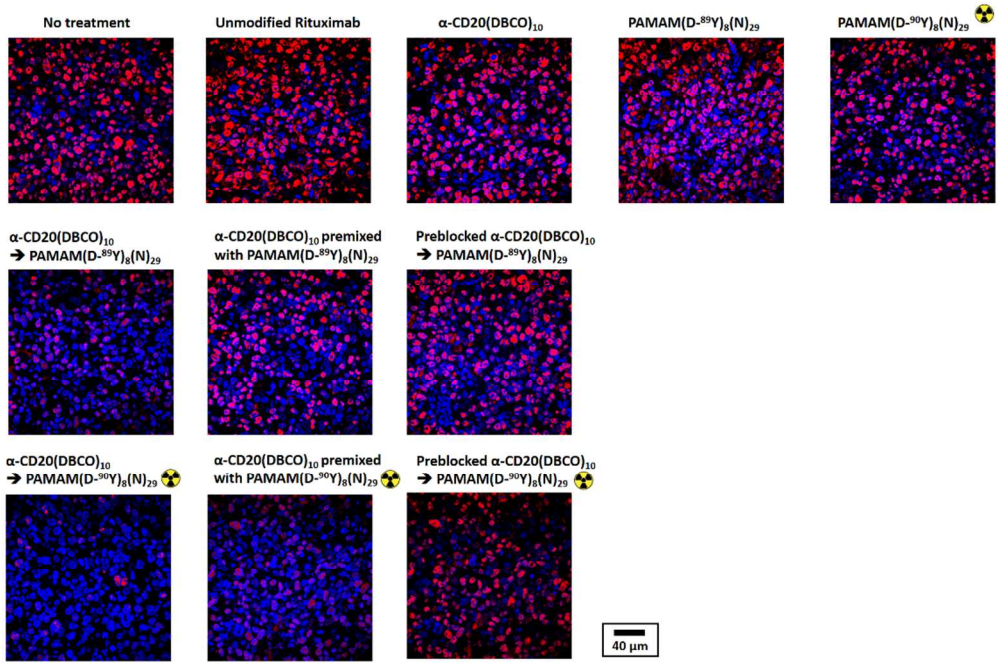

Figure S35. Representative CLSM images of anti-PCNA antibody-stained tumor sections after different treatments. All nuclei were stained with DAPI (blue fluorescence). The intense red fluorescence nuclei were PCNA-positive proliferating nuclei.

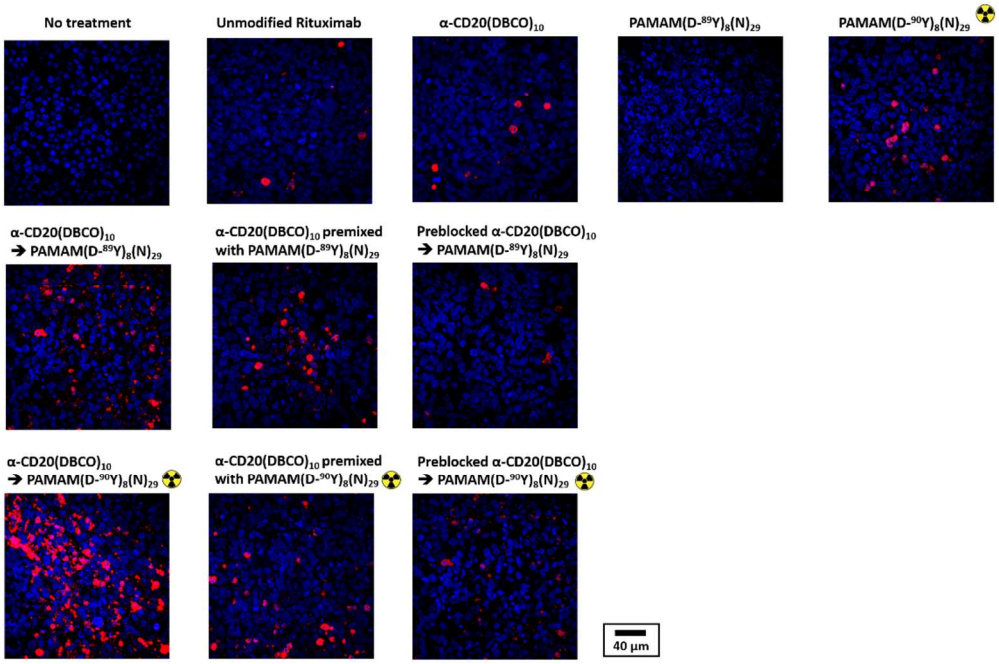

Figure S36. Representative CLSM images of anti-caspase 3 antibody-stained tumor sections after different treatments. All nuclei were stained with DAPI (blue fluorescence). The strong red fluorescence were caspase 3-positive cells.

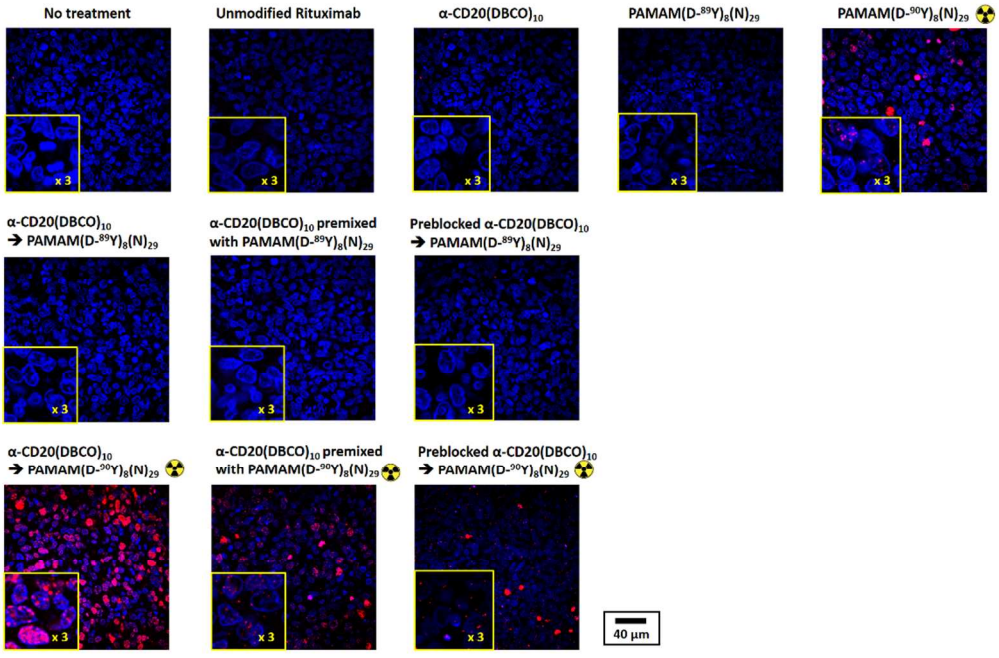

Figure S37. Representative CLSM images of anti-γ-H2AX antibody-stained tumor sections after different treatments. All nuclei were stained with DAPI (blue fluorescence). The strong red fluorescence foci labeled the DNA double-stand break.

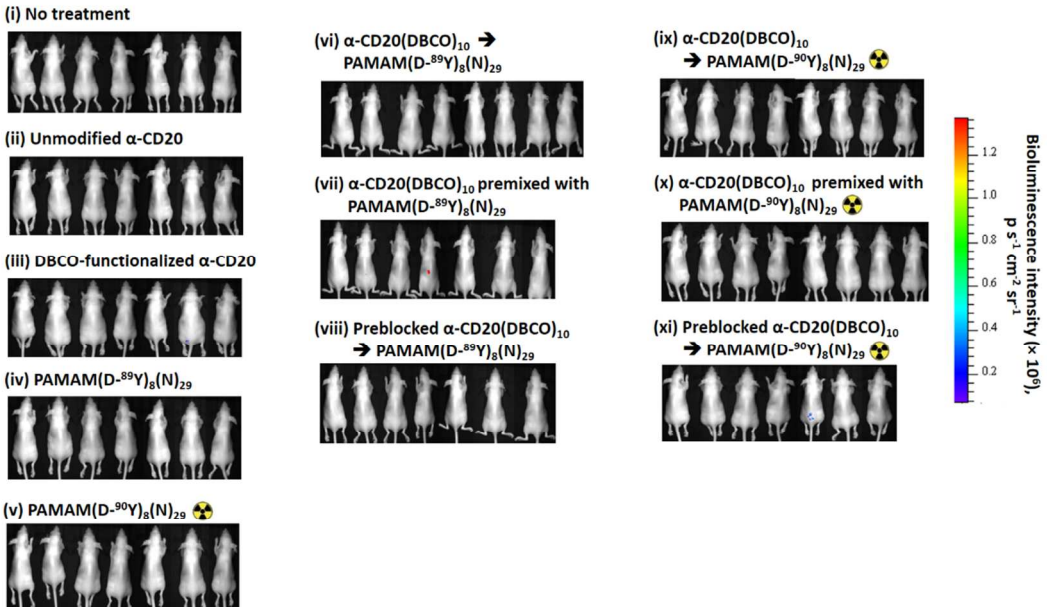

Figure S38. Whole-body *in vivo* bioluminescence images of mice in different treatment and control groups recorded before xenotransplantation (i.e., Day 0) of Raji-Luc cells (*via* i.v. tail vein injection of 2×10^6 Raji-Luc cells). Each mouse was intraperitoneally administrated with 3 mg firefly D-luciferin 15 min before bioluminescence imaging.

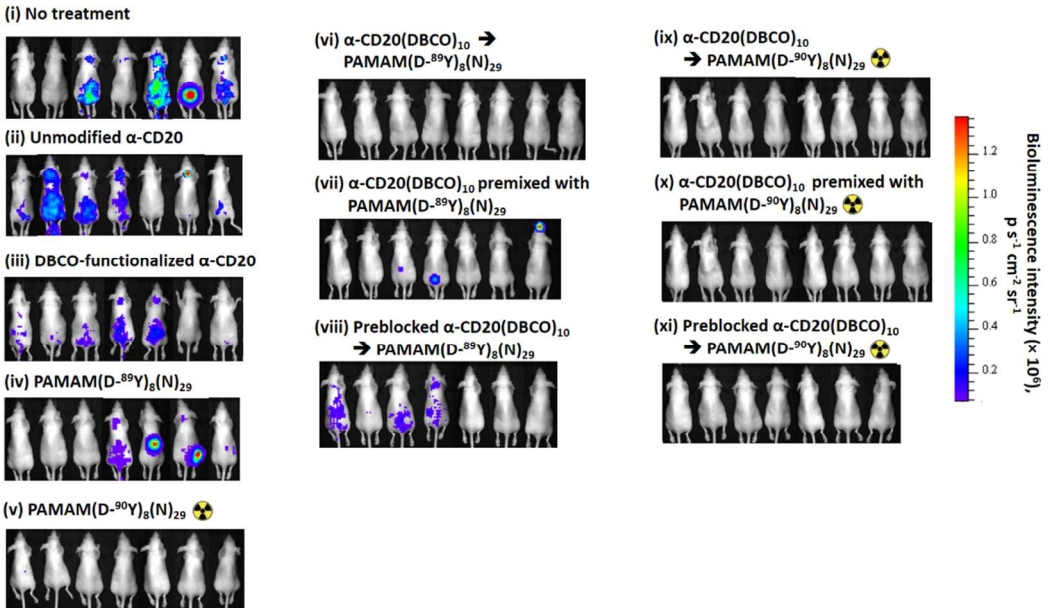

Figure S39. Whole-body *in vivo* bioluminescence images of mice in different treatment and control groups recorded 19 days post-xenotransplantation. Each mouse was intraperitoneally administrated with 3 mg firefly D-luciferin 15 min before bioluminescence imaging.

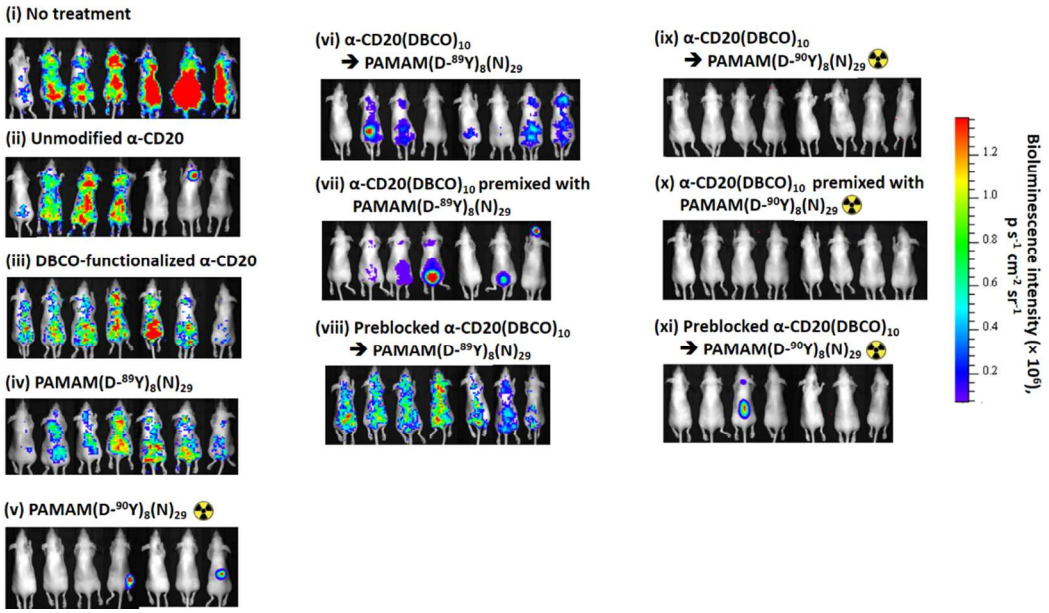

Figure S40. Whole-body *in vivo* bioluminescence images of mice in different treatment and control groups recorded 25 days post-xenotransplantation. Each mouse was intraperitoneally administrated with 3 mg firefly D-luciferin 15 min before bioluminescence imaging.

Figure S41. Whole-body *in vivo* bioluminescence images of mice in different treatment and control groups recorded 32 days post-xenotransplantation. Each mouse was intraperitoneally administrated with 3 mg firefly D-luciferin 15 min before bioluminescence imaging.

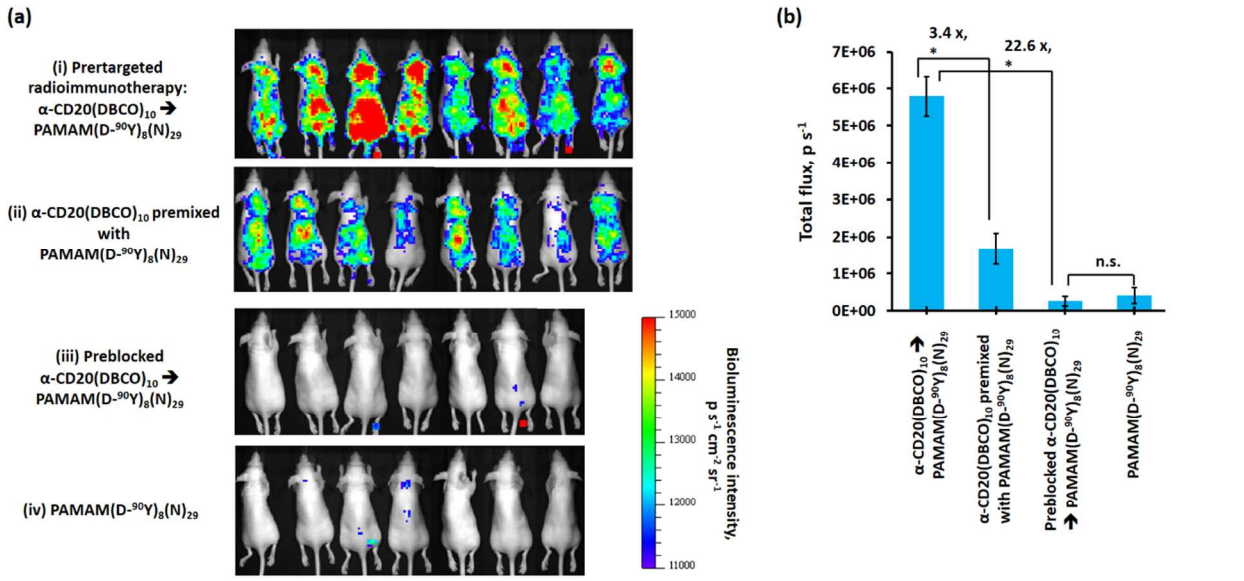

Figure S42. Cerenkov luminescence images of mice in different PAMAM(D-^{90}Y)$_8$(N)$_{29}$ treatment groups recorded 6 days after the second (final) i.v. administration of ^{90}Y-labeled dendrimer (19 days post-xenotransplantation). Cerenkov luminescence imaging was performed in the absence of D-luciferin. (N.B. * denotes $p < 0.05$.)

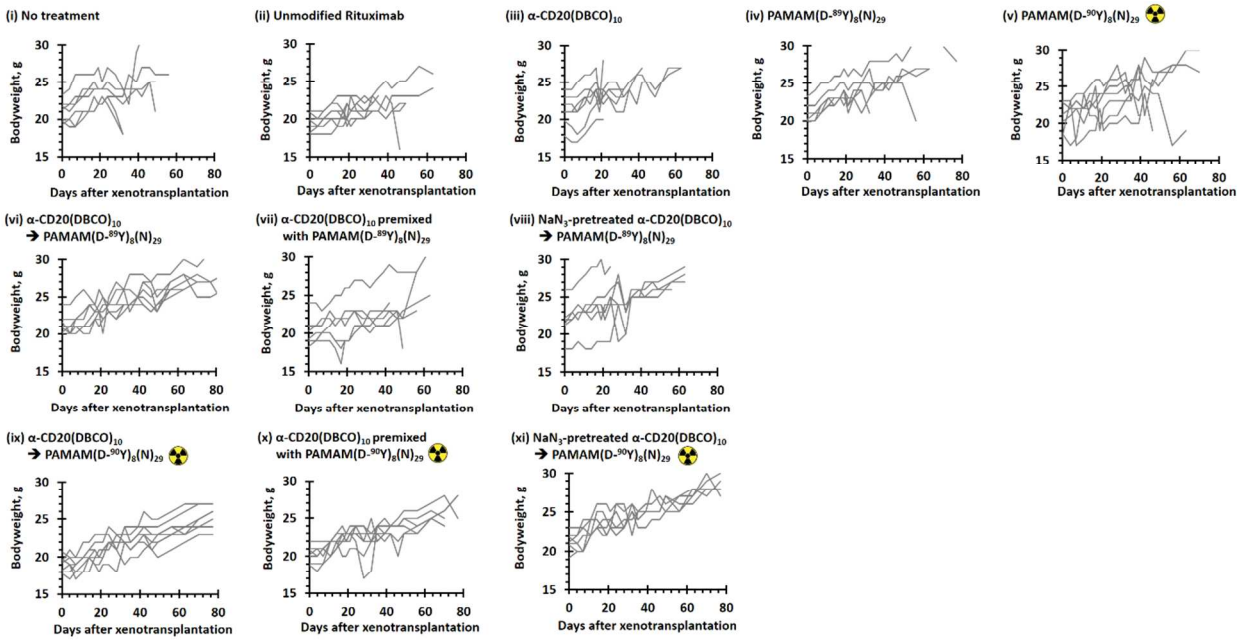

Figure S43. Bodyweight of individual Raji-Luc xenotransplanted mice recorded first 80 days after xenotransplantation.

SUPPORTING TABLE

	Reference range	PBS (Control)	Unmodified Rituximab[1]	α-CD20(DBCO)$_{10}$[1]	PAMAM(D-^{89}Y)$_8$(N)$_{29}$[2]	Preblocked α-CD20(DBCO)$_{10}$ followed by PAMAM(D-^{89}Y)$_8$(N)$_{29}$[3]	α-CD20(DBCO)$_{10}$ followed by PAMAM(D-^{89}Y)$_8$(N)$_{29}$[3]	α-CD20(DBCO)$_{10}$ premixed with PAMAM(D-^{89}Y)$_8$(N)$_{29}$[3]
Hematological Toxicity								
RBC, M/uL	8.9 ± 1.4	8.3 ± 0.1	8.9 ± 0.2	8.6 ± 0.2	8.5 ± 0.1	8.6 ± 0.3	8.3 ± 0.2	7.9 ± 0.3
HGB, g/dL	14.7 ± 2.2	13.0 ± 0.3	13.9 ± 0.3	13.8 ± 0.3	13.4 ± 0.3	13.5 ± 0.4	13.5 ± 0.4	12.4 ± 0.4
MCV, fL	56.1 ± 4.6	48.6 ± 0.3	48.2 ± 0.7	50.3 ± 0.7	49.4 ± 0.7	51.3 ± 0.8	50.1 ± 1.0	47.7 ± 0.6
MCH, pg	16.5 ± 1.0	15.7 ± 0.3	15.7 ± 0.1	16.0 ± 0.2	15.7 ± 0.3	15.7 ± 0.2	16.2 ± 0.1	15.8 ± 0.1
MCHC, g/dL	29.5 ± 2.8	32.3 ± 0.4	32.6 ± 0.2	31.8 ± 0.3	31.8 ± 0.3	30.6 ± 0.1	32.3 ± 0.4	33.2 ± 0.2
RET#, K/uL	338.3 ± 140.5	425.8 ± 22.4	394.4 ± 17.0	400.7 ± 24.4	398.7 ± 31.8	387.1 ± 67.7	460.3 ± 41.4	422.0 ± 24.5
PLT, K/uL	1538.9 ± 4006	1315.0 ± 78.1	1302.3 ± 67.7	1146.5 ± 112.2	1082.3 ± 71.9	1106.8 ± 50.5	752.3 ± 223.5*	917.5 ± 143.6*
PDW, fL	5.9 ± 0.4	6.9 ± 0.1	7.2 ± 0.2	7.2 ± 0.1	7.1 ± 0.1	7.3 ± 0.2	7.2 ± 0.2	7.1 ± 0.2
MPV, fL	5.1 ± 0.4	6.2 ± 0.1	6.3 ± 0.1	6.4 ± 0.1	6.4 ± 0.1	6.5 ± 0.1	6.6 ± 0.1	6.3 ± 0.2
WBC, K/uL	3.8 ± 0.8	3.4 ± 0.6	5.6 ± 0.2	5.6 ± 0.7	4.1 ± 0.8	6.2 ± 1.0	5.2 ± 1.2	7.1 ± 0.7
NEUT#, K/uL	0.9 ± 0.4	0.6 ± 0.1	0.8 ± 0.1	0.9 ± 0.1	0.7 ± 0.1	1.1 ± 0.2	0.6 ± 0.1	1.5 ± 0.2
LYMPH#, K/uL	2.6 ± 0.7	2.6 ± 0.6	4.6 ± 0.3*	4.4 ± 0.6*	3.1 ± 0.7	4.7 ± 0.7*	4.4 ± 1.1*	5.2 ± 0.7*
MONO#, K/uL	0.1 ± 0.0	0.1 ± 0.0	0.1 ± 0.0	0.2 ± 0.0	0.2 ± 0.1	0.3 ± 0.1	0.1 ± 0.0	0.3 ± 0.1
EO#, K/uL	0.2 ± 0.2	0.1 ± 0.0	0.1 ± 0.0	0.1 ± 0.0	0.1 ± 0.0	0.2 ± 0.0	0.1 ± 0.0	0.1 ± 0.0
BASO#, K/uL	0.04 ± 0.05	0.01 ± 0.00	0.02 ± 0.01	0.01 ± 0.00	0.01 ± 0.01	0.02 ± 0.01	0.01 ± 0.01	0.01 ± 0.00
Hepatotoxicity								
ALT, U/L	45.1 ± 16.1	32.3 ± 5.2	10.8 ± 5.1	16.3 ± 4.0	19.8 ± 3.9	17.8 ± 2.1	15.8 ± 1.7	14.0 ± 1.6
AST, U/L	80.6 ± 67.3	37.8 ± 4.4	30.5 ± 4.2	30.0 ± 4.3	32.3 ± 2.1	34.3 ± 5.0	31.5 ± 7.8	55.8 ± 27.1
Nephrotoxicity								
BUN, mg/dL	14.7 ± 4.0	23.5 ± 1.2	19.8 ± 1.7	23.5 ± 1.6	23.3 ± 1.0	20.8 ± 1.9	23.0 ± 1.1	24.0 ± 3.0
Creatinine, mg/dL	0.3 ± 0.1	0.3 ± 0.0	0.2 ± 0.0	0.3 ± 0.0	0.3 ± 0.0	0.3 ± 0.0	0.3 ± 0.0	0.3 ± 0.0

Table S1. In vivo toxicities of α-CD20(DBCO)$_{10}$ and PAMAM(D-^{89}Y)$_8$(N)$_{29}$ determined in healthy CD1 mice. The reference ranges were provided by Charles River Laboratories (https://www.criver.com/sites/default/files/Technical%20Resources/CD-1%C2%A0IGS%20Mouse%20Model%20Information%20Sheet.pdf).", (N.B. [1] 12 mg/kg α-CD20; [2] 40 mg/kg PAMAM(D-^{89}Y)$_8$(N)$_{29}$; [3]12 mg/kg mouse α-CD20 plus 40 mg/kg PAMAM(D-^{89}Y)$_8$(N)$_{29}$; RBC = red blood cell count; HGB = hemoglobin count; MCV = mean corpuscular volume; MCH = hemoglobin amount per red blood cell; MCHC = mean corpuscular hemoglobin concentration; RET = reticulocytes count; PLT = platelet count; PDW = platelet distribution width; MPV = mean platelet volume; WBC = white blood cell count; NEUT = neutrophils count; LYMPH = lymphocytes count; MONO = mononucleosis count; EO = eosinophilia count; BASO = basophils count; ALT = alanine aminotransferase; AST = aspartate aminotransferase; BUN = blood urea nitrogen. n = 5 per group. * denotes abnormal.)